

Uncovering blue diffuse dwarf galaxies

Bethan L. James,¹★ Sergey Kaposov,¹ Daniel P. Stark,² Vasily Belokurov,¹
Max Pettini¹ and Edward W. Olszewski²

¹*Institute of Astronomy, University of Cambridge, Madingley Road, Cambridge CB3 0HA, UK*

²*Steward Observatory, The University of Arizona, 933 N Cherry Ave, Tucson, AZ 85721, USA*

Accepted 2015 January 23. Received 2015 January 19; in original form 2014 October 3

ABSTRACT

Extremely metal poor (XMP) galaxies are known to be very rare, despite the large numbers of low-mass galaxies predicted by the local galaxy luminosity function. This paper presents a subsample of galaxies that were selected via a morphology-based search on Sloan Digital Sky Survey images with the aim of finding these elusive XMP galaxies. By using the recently discovered XMP galaxy, Leo P, as a guide, we obtained a collection of faint, blue systems, each with isolated H II regions embedded in a diffuse continuum, that have remained optically undetected until now. Here we show the first results from optical spectroscopic follow-up observations of 12 of ~ 100 of these blue diffuse dwarf (BDD) galaxies yielded by our search algorithm. Oxygen abundances were obtained via the direct method for eight galaxies, and found to be in the range $7.45 < 12 + \log(\text{O}/\text{H}) < 8.0$, with two galaxies being classified as XMPs. All BDDs were found to currently have a young star-forming population (< 10 Myr) and relatively high ionization parameters of their H II regions. Despite their low luminosities ($-11 \lesssim M_B \lesssim -18$) and low surface brightnesses ($\sim 23\text{--}25$ mag arcsec $^{-2}$), the galaxies were found to be actively star forming, with current star formation rates between 0.0003 and $0.078 M_{\odot} \text{ yr}^{-1}$. From our current subsample, BDD galaxies appear to be a population of non-quiescent dwarf irregular galaxies, or the diffuse counterparts to blue compact galaxies and as such may bridge the gap between these two populations. Our search algorithm demonstrates that morphology-based searches are successful in uncovering more *diffuse* metal-poor star-forming galaxies, which traditional emission-line-based searches overlook.

Key words: galaxies: abundances – galaxies: dwarf – galaxies: evolution – galaxies: irregular – galaxies: star formation.

1 INTRODUCTION

In order to further our understanding of the early Universe, we continually search for galaxies whose gas shows little or no trace of chemical evolution. Exploration of such pristine environments can provide insight into early galaxy formation and the properties of low-metallicity stars, along with constraints on theories of stellar evolution, the early enrichment of the pre-galactic medium, and studies of primordial elements (Skillman et al. 2013). Advancements continue to be made in this field, as searches now extend back to 400 Myr after the big bang (Coe et al. 2013) and candidates with photometric redshifts between $z \sim 9$ and 10 are frequently being detected (e.g. Zheng et al. 2012; Ellis et al. 2013; Oesch et al. 2013). However, due to their intrinsic faintness, very limited constraints can be extracted from such systems and we instead rely on the most unenriched galaxies in the *local* Universe to provide a valuable

means of constraining the early star formation, and consequently complement the ongoing high- z searches.

Unfortunately metal-poor objects are very rare, especially those belonging to the class of *extremely* metal poor (XMP) galaxies (defined as having $12 + \log(\text{O}/\text{H}) < 7.65$, less than one-tenth solar using the solar oxygen abundance of Asplund et al. 2009). For many decades, IZw18 ($12 + \log(\text{O}/\text{H}) = 7.18 \pm 0.03$ or $1/31 Z_{\odot}$; Legrand et al. 2000) and SBS 0335–052W ($12 + \log(\text{O}/\text{H}) = 7.12 \pm 0.03$ or $1/37 Z_{\odot}$; Izotov, Thuan & Guseva 2005) have held the record for the lowest metallicities and, at present, only 129 XMPs can be found in the literature (see Morales-Luis et al. 2011, for a compilation). Whilst their observed rarity is in part due to their inherent low luminosities (as demonstrated by the luminosity–metallicity, L – Z , relation; e.g. Lequeux et al. 1979; Skillman, Kennicutt & Hodge 1989; Garnett 2002), it is also in contradiction with the large number of low-mass galaxies predicted by the local galaxy luminosity function. This suggests that a large population of XMP galaxies still remains undetected.

* E-mail: bjames@ast.cam.ac.uk

The search for XMP galaxies has thus far focused primarily on surveying emission line galaxies. An up-to-date summary of such surveys can be found in Skillman et al. (2013), from which it is clear that although considerable effort has been spent in increasing the number of XMPs, the resultant yield has been very low. For example, of one million Sloan Digital Sky Survey (SDSS) Data Release 7 (DR7) spectra, there are only 15 candidates with $12 + \log(\text{O}/\text{H}) < 7.35$ within the Local Volume (Izotov et al. 2012). The low yield from these spectroscopic surveys is partly due to their design: they require naturally low surface brightness objects to have high surface brightness H II regions for detectability and abundance analysis.

An alternative strategy is to instead base the search criteria on L - Z relationship itself. Surveys of nearby, low-luminosity galaxies, and blind H I surveys have both been successful in detecting several XMPs (e.g. Skillman et al. 1989; van Zee 2000a; Pustilnik, Kniazev & Pramskij 2005; Cannon et al. 2011; Haynes et al. 2011; Tollerud et al. 2015), and in fact it was one discovery of this kind that gave rise to the sample of galaxies presented here. Via its H I signature alone, Leo P, a nearby dwarf irregular (dIrr) galaxy, was recently brought to light through the Arecibo Legacy Fast ALFA (ALFALFA) survey (Giovanelli et al. 2013). Whilst its H I properties were consistent with it being a ‘ultracompact high-velocity cloud’, optical spectroscopic follow-up by Skillman et al. (2013) revealed that Leo P was in fact one of the most metal-poor galaxies ever observed, with $12 + \log(\text{O}/\text{H}) = 7.17 \pm 0.04$ ($\sim 1/34 Z_{\odot}$).

Along with its extremely low metallicity, Leo P’s diffuse morphology and low surface brightness ($\mu_v = 24.5 \pm 0.6$ mag arcsec $^{-2}$; McQuinn et al. 2013) are atypical of most XMPs. The majority of low-metallicity galaxies are compact in nature, with only one or two bright H II regions dominating their structure and are often found to have a cometary or tadpole-shaped morphology (Papaderos et al. 2008; Morales-Luis et al. 2011; Sánchez Almeida et al. 2013). Leo P, on the other hand, consists of randomly distributed H II regions embedded within very low surface brightness emission. This lead us to speculate about how common this unconventional morphology may be amongst XMPs and whether we should be focusing on morphology rather than emission line properties when searching optical surveys for XMPs.

With the aim of answering this question, we undertook a systematic search in the Sloan source catalogue based on the morphology of Leo P (full details are given below). The result is a collection of faint, blue systems, each with isolated H II regions embedded in a diffuse continuum. We show a subsample of these ‘blue diffuse dwarfs’ (BDDs) in Fig. 1. In this publication, we present the first results from our ongoing optical spectroscopic follow-up of the sample. Whilst our spectroscopic survey is far from complete, we take this opportunity to introduce this previously optically undetected sample of galaxies to the community via their emission line and morphological properties.

The paper is structured as follows. In Section 2 we describe our methodology for generating the catalogue of BDDs. In Section 3 we provide information concerning the optical spectroscopic follow-up data, which are then presented in Section 4. In Section 5 we use the spectra to calculate the chemical abundances for each target, along with several emission line properties in Section 6 [i.e. star formation rate (SFR), luminosity, ionization parameter, and age of the current stellar population]. In Section 7 we use these properties to assess where BDDs lie in relation to current dwarf populations and discuss the morphological properties of the sample in Section 8. In Section 9 we summarize our findings and discuss the nature of BDDs and present our conclusions in Section 10.

2 SELECTION OF GALAXIES

The selection strategy of galaxies for this paper was primarily motivated by the morphology of recently discovered Leo P dwarf galaxy. While discovered using radio data, the galaxy is actually visible in the SDSS images as a very diffuse low surface brightness cloud with a couple of stellar-like H II regions. Thus we have devised a search method which looks for objects which are morphologically similar to Leo P in the photometric SDSS data base. For this paper we used the data from SDSS Data Release 9 (DR9; Ahn et al. 2012). The SDSS catalogues were queried from local SQL data base. The spatial queries to the data base were handled using q3c (Koposov & Bartunov 2006).

It is important to point out that the SDSS photometric pipeline was not designed to deal with morphologically complicated objects like Leo P, so for example the extended low surface brightness areas of such galaxies are often deblended as separated sources; some of the H II regions are labelled as extended sources, while some others as point sources. Furthermore, when searching for low surface brightness objects the diffraction spikes and glares from bright stars provide significant contamination of candidate lists. These problems complicate the search significantly and in the end limit the automation of the process. The main selection criteria adopted were the following.

- (i) Presence of blue point sources $-0.5 < (g - r)_0 < 1$, $-2 < (r - i)_0 < 0$ consistent with H II regions. In order to avoid artefacts from bright stars, we required that the SDSS photometric flags for these objects would not have SUBTRACTED and SATURATED fields set.¹ The objects having higher density of such sources within 10, 20, 30 arcsec were ranked higher.
- (ii) Presence of one or several of faint extended sources (θ) within 10, 20, 30 arcsec.
- (iii) Absence of bright (modelmag $_g < 18$) galaxy nearby.
- (iv) Absence of known LEDA² (Makarov et al. 2014) source or bright UCAC³ star nearby.
- (v) High galactic latitude.

These search criteria yielded hundreds of candidates (including Leo P and many known nearby star-forming dwarf galaxies). We then inspected the list, removed artefacts and all known sources within NASA/IPAC Extragalactic Database (NED), while keeping the best cases to create a final list of ~ 100 low surface brightness star-forming dwarf galaxies. A small subset of these is reproduced in Fig. 1, and their most important properties are collected in Table 1. For simplicity, in this paper we refer to the individual objects as ‘KJ X’, where X is the identification number and KJ corresponds to ‘Koposov–James’.

To illustrate the importance of different cuts to produce a small list of candidates, we provide a summary of the number of different sources which ‘survive’ a few key stages of our selection.

- (i) The number of high latitude $|b| > 30$ primary SDSS sources with psfmag $_g < 21$ is ~ 58 million.
- (ii) After applying the $g - r$ and $r - i$ colour cuts listed above, the number of objects is reduced to ~ 2 million.
- (iii) If we require to have two or more sources satisfying our colour cut inside a 20-arcsec aperture, the number of objects is

¹ https://www.sdss3.org/dr8/algorithms/flags_detail.php

² Lyon-Meudon Extragalactic Database: <http://leda.univ-lyon1.fr/>

³ USNO CCD Astrograph Catalog: <http://www.usno.navy.mil/USNO/astrometry/optical-IR-prod/ucac>

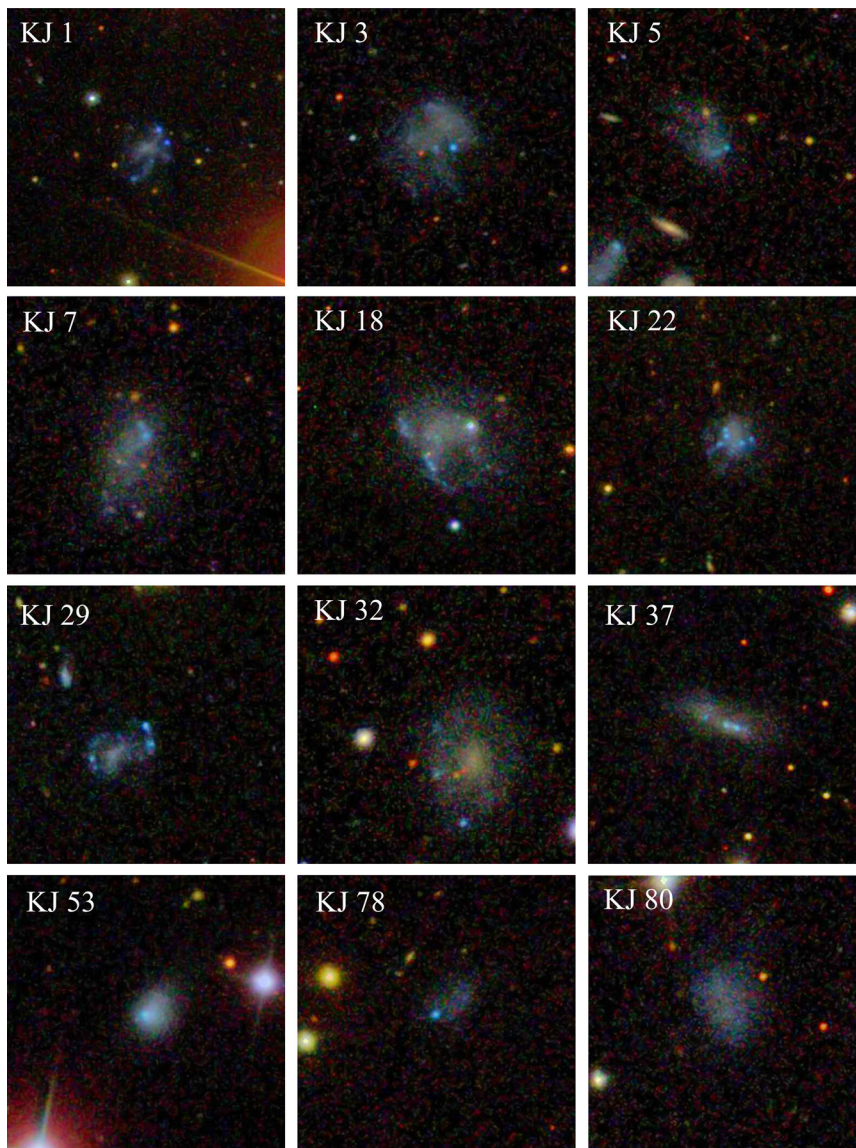


Figure 1. SDSS images of the BDD galaxies presented in this paper. Information on each object can be found in Table 1. Images were created from *gri*-band SDSS imaging and are ~ 102 arcsec on each side. North is up and east is to the left.

Table 1. BDDs galaxies in the current sample. Identifications according to SDSS and AGC are also given where available. Redshifts were derived from fitting all the emission lines seen within the spectrum and converted into distances using $H_0 = 67.8 \text{ km s}^{-1} \text{ Mpc}^{-1}$ (Planck Collaboration I 2014). SDSS images of each target can be found in Fig. 1. PA and T refer to the position angle of the slit orientation and the exposure time of the MMT observations, respectively.

Obj ID	SDSS ID	AGC ID	RA	Dec.	z	D (Mpc)	PA ($^\circ$)	T_{exp} (s)
KJ 1	J160753.65+090703.7	268137	16:07:53.652	09:07:03.76	0.02796	123	135	2×600
KJ 3	J141708.66+134105.5	242011	14:17:08.285	13:41:08.54	0.01611	72	20	2×1200
KJ 5	J085739.15+590256.4	–	08:57:39.155	59:02:56.41	0.00374	16	315	2×1200
KJ 7	J113453.11+110116.1	212838	11:34:53.455	11:01:11.16	0.00249	11	223	2×1200
KJ 18	J092127.17+072152.7	193816	09:21:27.173	07:21:50.70	0.00414	18	24	2×1200
KJ 22	J114109.10+244505.2	749439	11:41:08.885	24:45:04.75	0.01146	51	114	2×1200
KJ 29	J130110.39+365424.2	–	13:01:11.229	36:54:14.74	0.02252	100	105	1×950
KJ 32	J021111.29+281618.9	123128	02:11:10.356	28:16:09.84	0.01436	63	175	2×1200
KJ 37	J062538.13+655228.0	–	06:25:38.140	65:52:28.31	0.01387	61	20	3×1200
KJ 53	J115754.21+563816.7	–	11:57:54.213	56:38:16.76	0.00107	5	135	2×1200
KJ 78	J092036.41+494031.3	–	09:20:36.480	49:40:30.94	0.00159	7	64	3×1200
KJ 80	J092603.64+560915.5	–	09:26:03.600	56:09:15.48	0.00251	11	73	1×1200

reduced to $\sim 50\,000$ or ~ 8300 if we require having more than three objects.

(iv) After requiring not to have objects with SATURATED or SUBTRACTED photometric flags, those numbers reduce to 34 000 and 6400, respectively.

Further cuts, such as cross-match with LEDA, UCAC as well as bright galaxies ($\text{modelmag}_g < 18$) remove the residual contamination of the list from ‘big’ galaxies and artefacts from bright stars, and reduce the list of candidates to manageable size.

Our objects were additionally cross-referenced with the catalogue of 21 cm H I line sources of Haynes et al. (2011), consisting of 15 855 sources detected within 40 per cent of the ALFALFA survey (Giovanelli et al. 2005). Six of the 12 objects presented here are detected within the H I survey (KJ 1, 3, 7, 18, 22, and 32) and we utilize the H I masses presented in Haynes et al. (2011) for these galaxies in Section 8. The Arecibo General Catalogue (AGC) identification numbers for these galaxies are listed in Table 1. Furthermore, the optical-photometry-based properties of KJ 7 have been reported by Huang et al. (2012), who classified this object as a ‘dwarf’ according to the ALFALFA criteria. Overall, with respect to our entire sample, we find that ~ 20 per cent of our objects have a H I detection within the ALFALFA survey.

It should also be noted that one galaxy within our sample, KJ 53, already exists within the sample of XMPs presented by Morales-Luis et al. (2011) (object 18 in their table 1). This overlap between the two selection techniques may result from the fact that this particular object (i) lies at the closest distance within our current sample and (ii) is the most compact in nature. Being photometry driven, our selection criteria typically result in more distant and diffuse objects than those previously detected, although some degree of overlap is expected (and corrected for).⁴

3 OBSERVATIONS AND DATA REDUCTION

The galaxies studied here are listed in Table 1 in order of KJ number, along with some of their general properties such as their coordinates and redshift. Spectroscopic observations were obtained for each galaxy with the MMT Blue-Channel Spectrograph on the nights of 2014 January 27–28, and objects were chosen on account of their visibility during these nights. Observations were made using the medium-resolution grating (300 grooves mm^{-1}), giving a spatial scale along the slit of 0.6 arcsec pixel^{-1} , a spectral range of 3500–8000 Å, and a spectral resolution of ~ 7 Å [full width at half-maximum (FWHM)]. Table 1 also provides information on the position angle (PA) of the spectrograph slit, and exposure times of the observations.

The processing of the spectra was performed using a custom pipeline written in PYTHON. The reduction steps were standard. The raw data were bias subtracted and flat-fielded. The wavelength calibration was performed using the arcs observed immediately after or before each science exposure. The sky spectrum was subtracted from each science frame. The spectra of science objects were extracted by summing the flux along the slit within some aperture; optimal extraction was not possible due to the complicated structure of the objects (multiple H II regions with different line ratios and galaxy continuum). The extracted spectra from multiple exposures were combined using weighted average together with σ -clipping

⁴ In this case of KJ 53, a direct method of abundance had not been measured or published within the literature and as such we felt it was beneficial to keep it within the Multiple Mirror Telescope (MMT) sample.

to exclude residuals from cosmic rays. The flux calibration of the spectra was performed using spectrophotometric standard stars observed throughout each night with the instrument set-up described above. Uncertainties resulting from flux calibration were estimated to be ~ 8 –12 per cent, which is incorporated into the error spectrum accordingly. This somewhat conservative error is applied in order to account for the effects of systematic uncertainties, e.g. less than photometric conditions etc. In order to minimize these errors, each target was observed at its parallactic angle if it fell below an airmass of ~ 1.1 during the observation. In the cases where multiple H II regions were clearly evident in the two-dimensional spectra, extraction profiles were adjusted to obtain separate spectra of each region. Such cases are denoted as ‘KJ X.1’, ‘KJ X.2’ etc.

4 THE SPECTRA

Fig. 2 shows a complete, flux-calibrated MMT spectrum for each galaxy within our sample (as detailed in Table 1). Each spectrum exhibits all the strong emission lines typical of star-forming galaxies, superimposed on a blue continuum. In some of the brighter objects, we also observe the typically fainter emission lines such as the He I optical recombination lines and high ionization lines of [S III] and [Ar III]. We also show three objects (KJ 29.1, 32.0, and 80.0) whose spectra were particularly faint and where H β was not detected at 3σ significance level. As such, we have decided not to include these three objects in the analysis described within this paper, and simply show them here for completeness purposes.

For each spectrum, we model the emission lines with a single Gaussian component (multiple Gaussian components were not required) to deduce their redshifts and total integrated line flux of each emission line. The resultant redshifts are given in Table 1, while the detected lines and their integrated line fluxes are listed in Table A1. Redshifts were found to range from $z \sim 0.001$ to 0.023. Line flux measurements and their uncertainties were obtained following the methodology outlined in James et al. (2014), which employs a Markov chain Monte Carlo (MCMC) method to fit all of the observed lines within each spectrum simultaneously (i.e. requiring the redshifts and line widths to be the same for all the lines fitted).

Table A1 lists all lines that were found to be above the 3σ detection limit. We also list the 3σ upper limits of undetected lines that we deem necessary for the abundance calculations described in Section 5 (e.g. [O III] $\lambda 4363$ and [N II] $\lambda 6585$). The upper limit measurements were obtained by integrating the error spectrum over the model profile width determined from the high signal-to-noise ratio (S/N) emission lines. For galaxies in which underlying stellar absorption was visible, i.e. those with equivalent width (EW)(H α) < 100 Å, Balmer line fluxes were corrected accordingly (in the case of H β , EWs of the underlying profiles were found to be 1–3 Å).

Table A1 also lists the dereddened fluxes along with the reddening values used to make this correction. Reddening was estimated from the observed $F(\text{H}\alpha)/F(\text{H}\beta)$ and $F(\text{H}\gamma)/F(\text{H}\beta)$ ratios (combined in a 3:1 ratio, respectively), adopting the case B recombination ratios (appropriate for gas with $T = 10\,000$ K and $N_e = 100 \text{ cm}^{-3}$) and the Large Magellanic Cloud (LMC) extinction curve (Fitzpatrick 1999). In cases where H γ was not detected, only the $F(\text{H}\alpha)/F(\text{H}\beta)$ ratio was employed. For two of our targets (objects KJ 1.1 and KJ 3) we adopt $E(B - V) = 0.0$ (i.e. zero reddening) because the Balmer decrements were slightly below the theoretical case B ratio; this is most likely due to the uncertainties in the flux calibration.

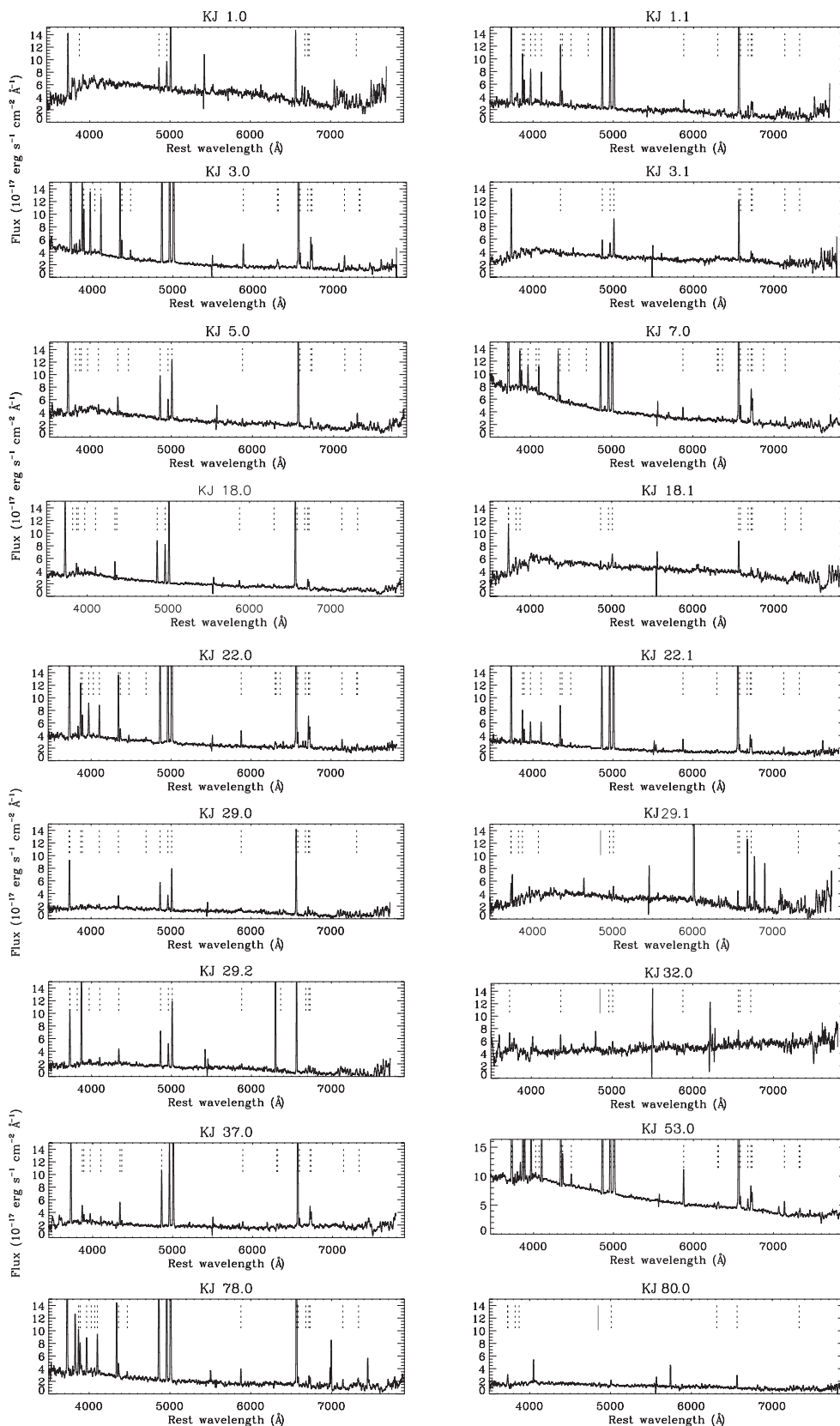


Figure 2. MMT spectra of the sample of BDD galaxies detailed in Table 1 and shown in Fig. 1. Wavelengths are given in the rest frame of each galaxy. Each spectrum has been smoothed with a 5-pixel boxcar for presentation purposes. The y-scale has been chosen to show the weakest emission lines. Dashed lines indicate emission lines detected in each spectrum, as listed in Table A1. Solid red lines indicate non-detected $H\beta$.

5 CHEMICAL ABUNDANCES

In order to calculate chemical abundances, we adopted the ‘direct method’ – i.e. a ‘direct’ measurement of the abundance of an element relative to H^+ based on the electron temperature (T_e) and density (N_e) of the gas and the extinction-corrected line fluxes. Ionic abundances are then converted into elemental abundances by adding up the different stages of ionization. It is this latter point that prevents us from measuring several different elemental abundances and we instead limit our calculations to O/H and N/O.⁵

When calculating the total elemental abundance, each of the ionic abundances is derived using the electron temperatures corresponding to the ionization ‘zone’ in which that ion dominates. For example, in order to calculate O^{2+}/H^+ , we calculate $T_e([O\ III])$ using the ratio of [O III] lines to an auroral line (e.g. $[O\ III](\lambda 5007 + \lambda 4959)/\lambda 4363$). In order to sample the lower ionization zone of the H II region, where O^+/H^+ resides, we require the auroral lines of [O II]. However, these are often weak and not detected, as is the case here. While $T_e([O\ II])$ can be calculated using empirical methods, a considerable amount of uncertainty exists due to outdated atomic data (energy levels, transition probabilities, and collision strengths). We therefore follow the methodology described in Nicholls et al. (2014) to calculate total oxygen abundances using equations derived from first principles and the most up-to-date atomic data.

The method itself is iterative, first calculating O^{2+}/H^+ using $T_e([O\ III])$ from the ratio described above. The O^{2+} is treated as the total oxygen abundance and used to calculate $T_e([O\ II])$ via an empirical relationship. The O^+/H^+ abundance can then be calculated using this value, and the [O II] $\lambda\lambda 3727, 3729$ doublet. The total O/H abundance is then recalculated ($O^+ + O^{2+}$) and the process repeated. The calculation converges within five iterations and involves case B emissivities and collision strengths for [O II] and [O III] based on their respective temperatures. Nicholls et al. (2014) also include a means of calculating $\log(N/O)$ by combining the methodology described above with the empirical formulae of Izotov et al. (2006), which account for the temperature dependencies of [O II] and [N II].

For each galaxy within our sample, we use the extinction-corrected line fluxes listed in Table A1 and the method described above to calculate $T_e([O\ III])$, $T_e([O\ II])$, O^+/H^+ , O^{2+}/H^+ , $12 + \log(O/H)$, and $\log(N/O)$ and list them in Table 2. In addition, we provide the mean N_e calculated using the density sensitive [O II] $\lambda\lambda 3727, 3729$ and [S II] $\lambda\lambda 6716, 6732$ doublets, and adopting $T_e([O\ II])$. Uncertainties in both values of T_e correspond to uncertainties in the relevant extinction-corrected fluxes, and are then propagated into the errors in the abundance values.

Accurate measurements of oxygen abundances (i.e. from detections of [O III] $\lambda 4363$) were obtained for nine out of 15 spectra (eight out of 10 objects). For those spectra where [O III] $\lambda 4363$ was considered a non-detection, we list the oxygen abundances as lower limits. Out of those for which values of T_e were obtainable, oxygen abundances were found to be in the range $7.45 < 12 + \log(O/H) < 8.0$, with two out of eight objects, KJ 53 and KJ 78, falling within the XMP classification ($12 + \log(O/H) < 7.65$).

Nitrogen-to-oxygen ratios were found to lie in the range $-1.60 < \log(N/O) < -1.39$, and are typical values for the metallic-

⁵ Whilst we regularly detect lines necessary to calculate S^+ , Ne^{3+} , and Ar^{3+} , the spectra are not deep enough to detect higher ionization stages and we would therefore be forced to employ ionization correction factors (ICFs). ICFs can often introduce large uncertainties (Kingsburgh & Barlow 1994) and we therefore refrain from using them within this study.

ity range of the sample (see e.g. López-Sánchez & Esteban 2010b, their fig. 11). This ratio, and its relation to metallicity, is discussed in more detail in Section 7.1.

With regards to homogeneity between multiple H II regions within the same system (i.e. KJ 1, 18, 22, 29, and 3), only KJ 22 has oxygen abundances that were measured with certainty in both regions and they are in agreement (within the uncertainties). The remaining candidates, where one is measured as a limit, are also consistent with having homogeneous oxygen abundances between the H II regions. Nebular abundances trace the youngest population and the chemical composition of the star-forming material, and so the observed chemical homogeneity may suggest that the gas within these objects is well mixed and/or star formation began at a similar time throughout.

6 EMISSION LINE PROPERTIES

6.1 Star formation rate and $L(H\alpha)$

We calculate the $H\alpha$ luminosity for each galaxy using the extinction-corrected $H\alpha$ line fluxes (Table A1) and the distances given in Table 1. $H\alpha$ luminosities are in the range $37.6 < \log(L_{H\alpha}) < 40.0$ erg s⁻¹, at the upper end of the range in luminosities seen in dIrrs (e.g. van Zee 2000b) and in the lower range of luminosities seen in blue compact dwarfs (BCDs; e.g. Gil de Paz, Madore & Pevunova 2003). $H\alpha$ EWs were also found to be typical of star-forming dwarf galaxies, falling within $20 \lesssim EW(H\alpha) \lesssim 300$ Å.

The $H\alpha$ luminosities were converted into a SFRs using the calibration of Kennicutt (1998). Both $L(H\alpha)$ and $SFR(H\alpha)$ are listed in Table 3. It can be seen that our current subsample of BDDs displays a rather large range in current SFRs, from 0.03×10^{-2} to 7.8×10^{-2} M_⊙ yr⁻¹, a range which is consistent with the range seen in local quiescent star-forming galaxies (i.e. < 0.1 M_⊙ yr⁻¹), and lower than in starburst galaxies (~ 0.1 – 1 M_⊙ yr⁻¹).

Overall, XMP galaxies are often found to have starbursting SFRs and as such are sometimes referred to as ‘emission line XMPs’. For these cases, Ekta & Chengalur (2010) associate the combination of high SFR and low metallicity with an infall of H I gas from the outskirts of the galaxy or accretion of metal-poor gas. However, our subsample of BDDs shows SFRs which are more reminiscent of ‘quiescent XMPs’ – a class of XMPs which became apparent with the discovery of Leo P, whose low luminosity ($L_{H\alpha} = 6.2 \times 10^{36}$ erg s⁻¹; Rhode et al. 2013) corresponds to a SFR of just 5×10^{-5} M_⊙ yr⁻¹. Skillman et al. (2013) suggest that in comparison to their emission line counterparts, quiescent XMPs may instead have formed through normal evolution of very low mass galaxies. Indeed, in line with Leo P, objects with particularly low SFRs (i.e. $< 1 \times 10^{-3}$ M_⊙ yr⁻¹) in our sample are also those with the lowest metallicities.

Using SFRs we can separate the currently observed BDD sample into two classes; those which are actively star forming ($SFR > 0.01$ M_⊙ yr⁻¹) and those with more quiescent SFRs (i.e. low but non-zero SFRs). On the one hand we have low-luminosity star-forming galaxies, while on the other we have (relatively) high-luminosity quiescent galaxies. For the former, it is their diffuse nature that has allowed them to pass below the detection threshold in previous emission line surveys.

6.2 Ionization strength

In order to assess the strength of the ionizing field within our subset of BDDs, we calculate the ionization parameter, U . This

Table 2. Ionic and elemental abundances for the BDD galaxies presented within this paper, derived from the emission line measurements given in Table A1. Electron density and temperatures are also listed.

ID	$N_e([O\ II],[S\ II])$ (cm^{-3})	$T_e([O\ III])$ (K)	$T_e([O\ II])$ (K)	O^+/H^+ ($\times 10^{-5}$)	O^{2+}/H^+ ($\times 10^{-5}$)	$12 + \log(O/H)$	$\log(N/O)$	$[O/H]^a$
KJ 1.0	590^{+2020}_{-290}	<17 470	<14 650	>3.69	>1.76	>7.74	>-1.74	>-0.95
KJ 1.1	720^{+1530}_{-400}	$15\,380 \pm 1960$	$12\,860 \pm 1370$	2.01 ± 0.87	3.18 ± 1.06	7.72 ± 0.16	-1.51 ± 0.21	-0.97 ± 0.16
KJ 3.0	110^{+520}_{-60}	$12\,930 \pm 2100$	$11\,360 \pm 1290$	4.27 ± 2.58	5.56 ± 3.12	7.99 ± 0.23	-1.60 ± 0.29	-0.70 ± 0.24
KJ 3.1	460^{+1700}_{-230}	<19 720	<16 250	>3.07	>0.79	>7.59	>-1.23	>-1.10
KJ 5.0	180^{+700}_{-130}	<15 430	<12 830	>3.77	>0.86	>7.67	>-1.69	>-1.02
KJ 7.0	1500^{+1180}_{-660}	$12\,880 \pm 1540$	$11\,330 \pm 950$	6.32 ± 2.58	3.60 ± 1.33	8.00 ± 0.16	-1.47 ± 0.20	-0.69 ± 0.17
KJ 18.0	690^{+2060}_{-340}	$16\,280 \pm 2770$	$13\,540 \pm 1990$	3.01 ± 1.62	1.62 ± 0.63	7.67 ± 0.20	-1.55 ± 0.22	-1.02 ± 0.20
KJ 18.1	2480^{+50}_{-1180}	<54 020	<44 710	>0.61	>0.14	>6.87	>-1.08	>-1.82
KJ 22.0	230^{+540}_{-130}	$12\,920 \pm 1390$	$11\,330 \pm 860$	4.26 ± 1.62	5.33 ± 1.83	7.98 ± 0.15	-1.49 ± 0.19	-0.71 ± 0.16
KJ 22.1	120^{+420}_{-70}	$13\,550 \pm 1580$	$11\,690 \pm 1020$	3.87 ± 1.57	4.18 ± 1.46	7.91 ± 0.16	-1.59 ± 0.20	-0.78 ± 0.17
KJ 29.0	320^{+1090}_{-250}	<15 960	<13 150	>2.91	>0.91	>7.58	>-1.60	>-1.11
KJ 29.2	1140^{+1750}_{-660}	<13 360	<11 380	>5.02	>1.72	>7.83	>-2.10	>-0.86
KJ 37.0	650^{+1950}_{-290}	$14\,930 \pm 2090$	$12\,720 \pm 1400$	3.88 ± 1.77	2.92 ± 1.06	7.83 ± 0.17	-1.49 ± 0.21	-0.86 ± 0.18
KJ 53.0	300^{+720}_{-160}	$16\,890 \pm 2290$	$13\,770 \pm 1750$	1.03 ± 0.47	1.80 ± 0.57	7.45 ± 0.15	-1.52 ± 0.19	-1.24 ± 0.16
KJ 78.0	380^{+760}_{-260}	$15\,020 \pm 1930$	$12\,420 \pm 1380$	1.64 ± 0.76	2.53 ± 0.86	7.62 ± 0.16	-1.39 ± 0.20	-1.07 ± 0.17

Note: $^a[O/H] \equiv \log(O/H)_{\text{gal}} - \log(O/H)_{\odot}$, where $\log(O/H)_{\odot}$ is from the solar composition value recommended by Asplund et al. (2009).

Table 3. Various properties of the sample of BDD galaxies: $H\alpha$ luminosity, SFR, ionization parameter (U), and the age of the current star-forming population determined from the EW of $H\beta$. A detailed description of each property can be found in Section 6.

ID	$L(H\alpha)$ ($\times 10^{38} \text{ erg s}^{-1}$)	SFR($H\alpha$) ($\times 10^{-2} M_{\odot} \text{ yr}^{-1}$)	$\log(U)$	Age (EW($H\alpha, H\beta$)) (Myr)
KJ 1.0 ^a	31.48 ± 3.59	2.49 ± 0.28	-3.01 ± 0.10	<11.81
KJ 1.1	98.20 ± 9.85	7.76 ± 0.78	-2.58 ± 0.11	6.63 ± 1.32
KJ 3.0	56.24 ± 8.96	4.44 ± 0.71	-2.50 ± 0.18	4.27 ± 0.67
KJ 3.1 ^a	6.70 ± 0.68	0.53 ± 0.05	-3.25 ± 0.07	<12.19 1.30
KJ 5.0 ^a	1.08 ± 0.12	0.09 ± 0.01	-3.19 ± 0.07	<9.85 0.84
KJ 7.0	0.99 ± 0.10	0.08 ± 0.01	-2.78 ± 0.13	6.09 ± 1.52
KJ 18.0	1.18 ± 0.13	0.09 ± 0.01	-2.96 ± 0.08	9.55 ± 0.91
KJ 18.1 ^{a,b}	0.39 ± 0.05	0.03 ± 0.00	-3.47 ± 0.08	<15.70
KJ 22.0	32.19 ± 3.40	2.54 ± 0.27	-2.52 ± 0.11	4.96 ± 1.09
KJ 22.1	20.03 ± 2.12	1.58 ± 0.17	-2.61 ± 0.10	6.06 ± 1.47
KJ 29.0 ^a	19.92 ± 2.07	1.57 ± 0.16	-3.13 ± 0.08	<9.96
KJ 29.2 ^a	31.34 ± 3.43	2.48 ± 0.27	-3.00 ± 0.09	<8.30
KJ 37.0	28.82 ± 3.62	2.28 ± 0.29	-2.79 ± 0.10	7.69 ± 1.50
KJ 53.0	0.47 ± 0.05	0.04 ± 0.00	-2.65 ± 0.09	7.23 ± 1.58
KJ 78.0	0.43 ± 0.04	0.03 ± 0.00	-2.61 ± 0.09	6.65 ± 1.74

Notes: ^aObject has lower limit oxygen abundance.

^bCalculated using $Z = 0.1 Z_{\odot}$ (the minimum metallicity allowed within the U parameter relation of Kewley & Dopita 2002).

dimensionless parameter represents the ratio of the density of ionizing photons per unit volume to the particle (atom plus ion) number density. The U -parameter is often quoted as q , where $U = q/c$, c being the speed of light. We estimate the value of U for each galaxy using the iterative equations of Kewley & Dopita (2002) together with the oxygen abundances listed in Table 2 and the $[O\ III] \lambda 5007/[O\ II] \lambda \lambda 3727, 3729$ ratios. Adopting the metallicity of each galaxy, we interpolate between the relevant equations of Kewley & Dopita (2002). The resultant U -parameters are given in Table 3, and range $-3.47 < \log(U) < -2.50$ ($7.0 < \log(q) < 7.9$). These are somewhat typical values for mid-to-low metallicity star-forming galaxies (see e.g. Dopita et al. 2013).

6.3 Current age of ionizing stellar population

We investigate the current age of the star-forming population via the luminosities of hydrogen recombination lines. $H\alpha$ and $H\beta$, in particular, provide an estimate of the ionizing flux present, assuming a radiation-bounded nebula (Schaerer & Vacca 1998). We therefore estimate the age of the latest star-forming episodes in each object via the Balmer line EW and its metallicity, and compare them with those predicted by the spectral synthesis code, STARBURST99 (Leitherer et al. 2010). Models were run at the full range of available metallicities (0.05, 0.2, 0.4, and $1 Z_{\odot}$), along with assumptions of an instantaneous burst, a Salpeter initial mass function (IMF), ‘standard’ Geneva tracks, and Paudruch–Hillier atmospheres. Only

models with zero rotation were employed due to the limited range in metallicities currently available for models with rotation. We interpolate between the models at the metallicity of each galaxy (Table 2), and assess the age of the current stellar population according to its EW($H\beta$) and EW($H\alpha$). We list the mean and difference of these two ages in Table 3.

Ages were found to range between 4.3 and 9.6 Myr, with a mean age of 6.6 ± 1.5 Myr (this does not account for galaxies for which lower limit oxygen abundances are available, as only upper limits can be calculated in these cases). Such young ages suggest that these BDDs are within the earlier stages of star formation or have recently undergone a burst of star formation. At this particular age, stellar populations are expected to be going through their Wolf–Rayet (WR) phase. While there are hints of WR signatures, i.e. the ‘WR bump’ at ~ 4690 Å in several of the objects (KJ 1.1, 3, 7, 22, and 29), the S/N of the spectra is not sufficient to quantify the population age more precisely. It is interesting to note, however, that WR features are not typically seen in XMP galaxies, even when the starburst is young (Shirazi & Brinchmann 2012).

7 DISCUSSION

In order to assess the role that BDDs play within the local population of galaxies we will compare the properties discussed in Sections 5 and 6 with those of other dwarf galaxies. We do note, however, that since only a small number of BDDs have been studied to date, such comparisons may suffer from low-number statistics.

We are particularly interested in how our current subset of BDDs compare to other low-metallicity dwarf galaxies and have therefore assembled a comparison sample consisting of the following: BCDs from Izotov et al. (2012); XMP galaxies [Leo P (Skillman et al. 2013), Leo A (van Zee & Haynes 2006), UGCA 292 (van Zee 2000a), DDO 68 (Pustilnik et al. 2005), SBS 1129+576 (Ekta, Chengalur & Pustilnik 2006; Guseva et al. 2003), SBS 1129+577 (Ekta et al. 2006), J2104–0035 and UGC 772 (Ekta, Chengalur & Pustilnik 2008), UM 133 and SDSS J011914 (Ekta & Chengalur 2010), HS 2134 (Pustilnik et al. 2006), and the sample of Morales-Luis et al. (2011)]; and low-luminosity dwarf galaxies of Berg et al. (2012). We also include nearby dwarf galaxies from the volume-limited survey by Karachentsev, Makarov & Kaisina (2013). In order to avoid discrepancies between metallicity measurements, we only include galaxies for which a direct measurement of the metallicity has been reported.

7.1 N/O versus oxygen abundance

A great deal of discussion regarding the relationship between the oxygen abundance and the N/O ratio exists in the literature, as such a relationship can be used to assess the chemical evolutionary age of a galaxy (see e.g. Skillman, Côté & Miller 2003; López-Sánchez & Esteban 2010a, and references therein). It was first thought that at extremely low metallicities N/O is constant with O/H, forming a narrow plateau which Izotov & Thuan (1999) attributed to XMPs currently undergoing their *first* burst of star formation (i.e. ages $\lesssim 40$ Myr) and nitrogen undergoing primary production by high-mass stars. However, as the number of low-metallicity objects has increased, the reality of such a narrow range of values of N/O has come to be questioned. For example, van Zee & Haynes (2006) reported a large scatter in N/O at low metallicities, which had been anticipated by Garnett (1990). The scatter may be due to the time delay between the release of oxygen from massive stars and primary nitrogen from low- and intermediate-mass stars as proposed by Vila

Costas & Edmunds (1993) (see also Pettini et al. 2008), or perhaps an infall of metal-poor gas in some galaxies (Amorín et al. 2012), but a full interpretation is still far from being established (Skillman et al. 2013; Zafar et al. 2014). At higher metallicities, the effects of secondary production are seen as N/O increases linearly with oxygen abundance.

As can be seen from Fig. 3, the values of N/O we have found in our sample of BDDs are comparable to those measured in other low-metallicity galaxies. The limited accuracy of our abundance determinations and limited sample size preclude firm conclusions concerning the reality of the scatter at the lowest metallicities. Rather we stress the future potential of BDD galaxies for addressing, and possibly resolving, this issue as they provide a firmer handle on the relationship in the low-metallicity regime.

7.2 Emission line diagnostics

In Fig. 4 we place the BDDs on the well-known emission line diagnostic diagram, $[N\text{ II}]/H\alpha$ versus $[O\text{ III}]/H\beta$. This diagram, first utilized by Baldwin, Phillips & Terlevich (1981) and Veilleux & Osterbrock (1987), separates galaxies with regards to their metallicity, strength of their ionizing radiation, and hardness of the ionizing radiation. In order to demonstrate this, we plot the emission line ratios of the SDSS galaxies in Fig. 4, which form the well-known ‘seagull’ shape – a branch of star-forming galaxies on the left and a branch of Seyfert/low-ionization nuclear emission-line region galaxies (LINERs) on the right. It can be seen from Fig. 4 that BCDs, due to their starburst and low-metallicity environments, tend to lie on the top-left branch of the star-forming galaxies. XMPs, on the other hand, tend to fall slightly below the BCDs, suggesting somewhat weaker ionizing radiation perhaps due to a more quiescent star-forming environment. In comparison to the other dwarf galaxies, the BDDs within our existing sample are quite tightly clustered and all lie towards the top of the star-forming branch and within the upper range of $[N\text{ II}]/H\alpha$ displayed by BCDs. Their distribution within the diagram suggests that they are objects consisting of low metallicity, highly ionized gas. However, in general BDDs do not seem to overlap with XMP galaxies.

8 MORPHOLOGICAL PROPERTIES AND STELLAR MASSES

Whilst our sample of BDDs is clearly dwarf galaxies, deciding which particular class of dwarf galaxies they belong to is somewhat difficult. Taking into account their irregular morphology, low metallicities, and current level of star formation, BDDs are most naturally placed within the dIrrs category. The different types of dIrrs have not been precisely defined, and classification is often based on their morphology and/or current rates of star formation.

Within the dIrr category we also have BCD galaxies – an extreme form of dIrr where star formation occurs in a few compact regions, and at an intense rate. BCDs, by definition, are compact – a term which refers more to the size of the high surface brightness component than the total optical size. Peak surface brightnesses of BCDs are significantly higher than most other dIrrs, with BCDs having $\mu_{B,\text{peak}} < 22$ mag arcsec $^{-2}$ (Gil de Paz et al. 2003). This is mostly due to the recent star-forming episodes within the BCDs, whereas the star formation in dIrrs is less recent and less active, causing them to be fainter and redder. Unfortunately, due to the highly irregular distribution of light throughout the BDD galaxies, we are at present unable to quantify the peak surface brightness

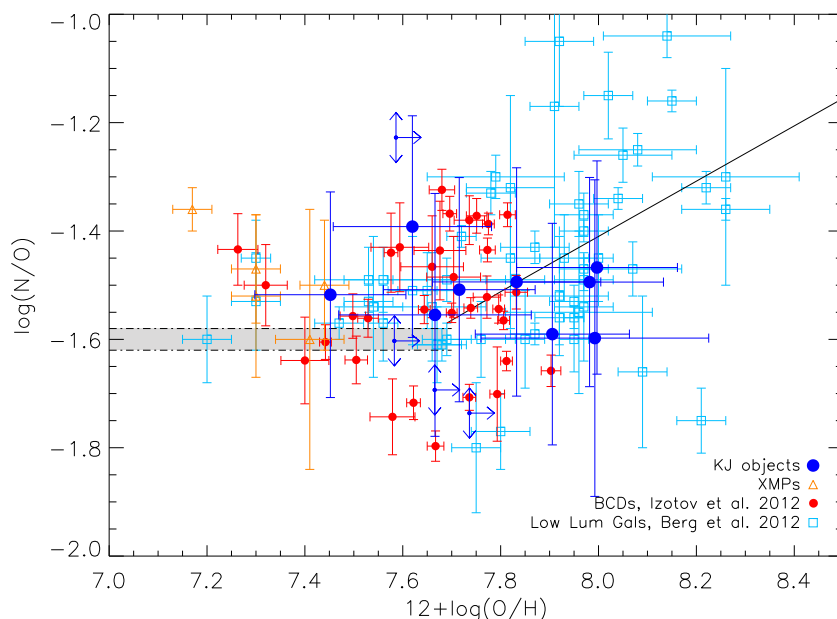


Figure 3. The relationship between metallicity and nitrogen-to-oxygen ratio in the low-metallicity regime. We show the results from our sample of BDD galaxies (i.e. KJ objects listed in Table 1, blue circles) and for comparison we plot the values measured in a sample of XMPs (see text for details), the recently compiled sample of BCDs by Izotov, Thuan & Guseva (2012), and the low-luminosity dwarf galaxies of Berg et al. (2012). The black solid line shows the relationship between $\log(N/O)$ and $\log(O/H)$ in the metallicity range $12 + \log(O/H) > 7.7$ derived by Berg et al. (2012) for low-luminosity galaxies, while the grey shaded region is the narrow N/O plateau proposed for XMPs by Izotov & Thuan (1999).

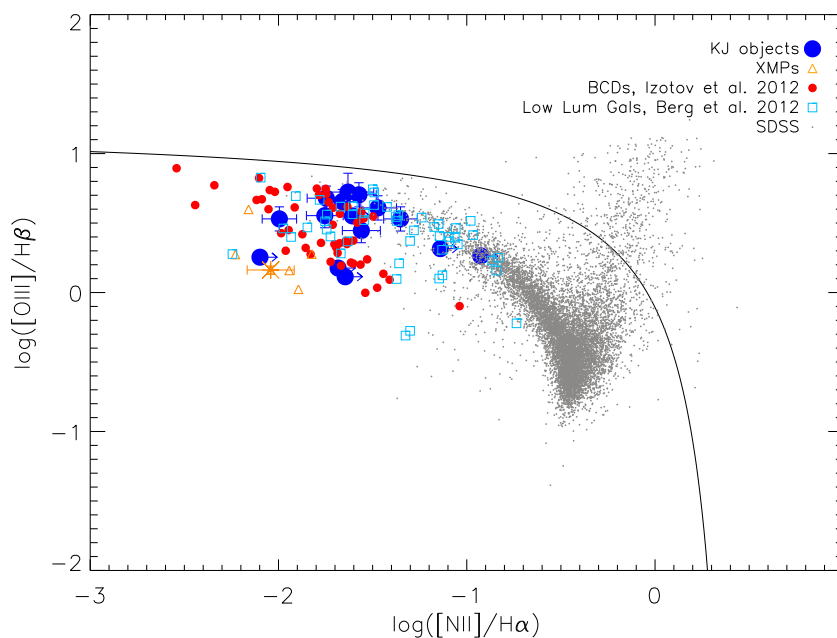


Figure 4. An emission line diagnostic diagram, showing $[O\ III]/H\beta$ versus $[N\ II]/H\alpha$, traditionally used to separate galaxies according to their metallicity, strength, and hardness of their ionizing radiation. In black we show the SDSS emission line galaxies (selected according to the criteria of Brinchmann, Kunth & Durret 2008), which form a branch of star-forming galaxies on the left, and Seyferts/LINERs on the right. The BDD galaxies (i.e. KJ objects listed in Table 1) tightly cluster towards the top part of the star-forming branch, suggesting they composed of low metallicity, highly ionized gas. For comparison, we also plot a selection of XMPs, BCDs, and low-luminosity dwarf galaxies (see text for details). The black solid line represents the ‘maximum starburst line’ of Kewley et al. (2001).

of our objects; this is something which we intend to achieve with better quality photometric observations.

We can however assess their effective surface brightness μ_B . To compute this parameter we calculate the total B -band magnitude and the half light radius of each galaxy from their g - and r -band

growth curves obtained from the SDSS images. To convert the g - and r -band magnitudes into the B band we use the relations from Lupton (2005). Both the absolute B -band magnitudes and effective surface brightnesses for the BDDs within the sample are listed in Table 4.

Table 4. Photometric properties of the BDD sample.

ID	M_B (mag)	μ_B (mag arcsec $^{-2}$)	$\log(M_*)$ (M_\odot)	$\log(M_{\text{HI}})$ (M_\odot)
KJ 1	-17.98	24.1	9.04	9.39
KJ 3	-17.14	24.4	8.90	9.40
KJ 5	-13.12	24.5	8.43	–
KJ 7	-13.28	24.3	7.48	7.60
KJ 18	-15.49	23.2	8.43	8.44
KJ 22	-15.92	23.5	8.32	8.77
KJ 29	-17.31	24.7	8.79	–
KJ 37	-16.24	24.4	8.69	–
KJ 53	-11.17	22.6	6.45	–
KJ 78	-10.72	24.6	6.52	–

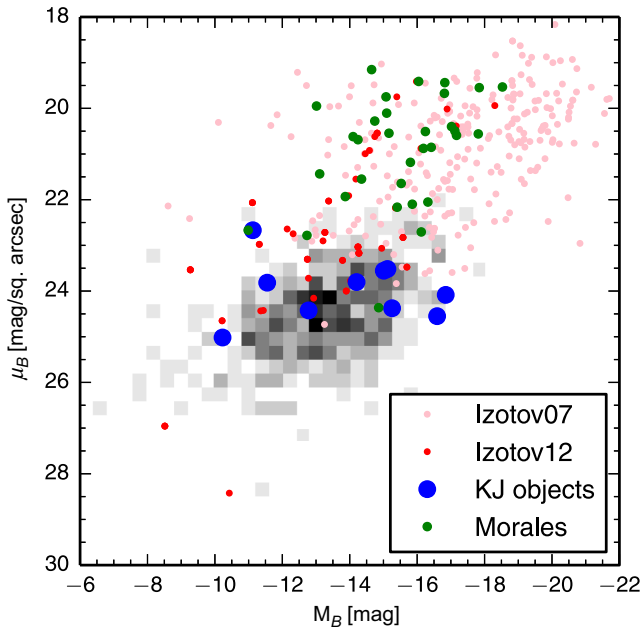


Figure 5. Absolute B -band magnitude versus effective B -band surface brightness for the BDD galaxies within our current sample (i.e. KJ objects listed in Table 1). We also overplot the SDSS-selected low-metallicity H II regions (Izotov, Thuan & Stasińska 2007) and XMP galaxies (Morales-Luis et al. 2011; Izotov et al. 2012), along with nearby dwarf galaxies from the volume-limited sample by Karachentsev et al. (2013) shown in grey-scale.

With the aim of putting the morphological properties of BDDs into context, in Fig. 5 we compare their magnitudes and surface brightnesses against those of other dwarf galaxies observed in the SDSS survey. By only using other SDSS dwarfs we can ensure consistency between the calculations M_B and μ_B , which we derive using the method described above. Our comparative sample consists of the XMPs of Morales-Luis et al. (2011), low-metallicity emission line galaxies of Izotov et al. (2012), low-metallicity H II regions of Izotov et al. (2007), and the volume-limited sample of Karachentsev et al. (2013). It can be seen that BDDs lie within the fainter end of low-metallicity dwarf galaxies, and overlap with the local dIrrs. Their position within the diagram suggests that BDDs could be the more distant analogues of local dwarf galaxies, which are currently undergoing or recently finished a burst of star formation. However, rather than the star formation occurring in compactly distributed H II regions, it occurs in a more diffuse manner and this leads to lower values of μ_B . As such, this separates BDDs from BCDs and XMPs and places them within the middle of the distribution,

suggesting that these systems could be a link between quiescent dIrrs and starbursting BCDs.

Using the g - and r -band colours, we can also make a crude estimation of the stellar mass, M_* , within the BDDs using the stellar mass-to-light ratio relation $(M/L)_i = 0.222 + 0.864 \times (g - r)$ from Bell et al. (2003). Stellar masses are found to range between $M_* \sim 0.03 \times 10^8$ and $\sim 11 \times 10^8 M_\odot$ (see last column of Table 4). This range encompasses the stellar masses of both dIrrs (see e.g. Lee et al. 2006) and BCDs (see e.g. Zhao, Gao & Gu 2013). It should be noted however that without infrared (IR) images such estimates are extremely uncertain (e.g. Gil de Paz et al. 2003; Zhao et al. 2013) and as such we refrain from including them in any further analysis of the population.

For comparison, in Table 4 we also list the H I masses for those galaxies detected within the ALFALFA survey, as presented in Haynes et al. (2011). Overall, it appears that the BDD’s baryonic mass is dominated by atomic gas, rather than their stars. This was also found to be the case for over half of the ALFALFA dwarfs presented in Huang et al. (2012). With regards to Leo P, $\log(M_{\text{HI}}/M_\odot) \sim 6$, the BDDs are 2–3 orders of magnitude more massive in H I.

9 WHAT ARE BDDs?

Overall, our current subset of BDD galaxies appears to be metal-poor, low surface brightness objects in the nearby Universe who are forming stars at rates that range from quiescent to semi-active. Whilst their current stellar populations are very young (< 10 Myr) we cannot rule out the possibility of an older, underlying population, as found in all BCDs (and XMPs) close enough for us to allow resolved stellar populations (e.g. Aloisi et al. 2007; Papaderos et al. 2008) and deep *Hubble Space Telescope* (HST) imaging of nearby dIrrs [e.g. Leo A, Cole et al. (2007); IC 1613, Skillman et al. (2014); DDO 210, Cole et al. (2014)]. While each of these properties make them very similar to other dwarf galaxies currently studied, their combination of non-zero SFR and diffuse morphology separate them somewhat. In Fig. 6 we plot the current SFR (derived from extinction-corrected H α emission) against M_B for BDDs, low-luminosity galaxies, a selection of XMPs, BCDs, and individual H II regions in low-metallicity galaxies. This plot is comparable to the popular SFR versus mass diagram used in studies of high-redshift galaxies. In SFR–luminosity space, it can be seen that BDD galaxies occupy a region between low-luminosity quiescent galaxies and bright starbursting BCD galaxies. BDDs do align with the individual H II regions of low-metallicity galaxies observed by Izotov et al. (2012), which were selected from SDSS-DR7 on the basis of having weak [O III] and [N II] emission lines relative to H β . Although, interestingly, most of low-metallicity host galaxies detected by Izotov et al. (2012) were already known in the literature – possibly because these systems have relatively higher surface brightnesses (Fig. 5).

On the one hand, BDDs have emission line properties that agree with various BCD criteria (e.g. Gil de Paz et al. 2003, and references therein). On the other hand, their morphological properties are more in-line with dIrrs (Fig. 5). It should be noted, however, that we base such comparisons purely on the range of properties observed within the small subset we have studied to date. Even so, with regards to their SFRs, our current sample of BDDs could be considered as a mixed bag of quiescent and semi-actively star-forming galaxies or, in other words, a mixture of dIrrs and low-luminosity BCDs. In comparison to BCDs, dIrrs are currently forming stars at an extremely low rate which will for the majority of time remain constant

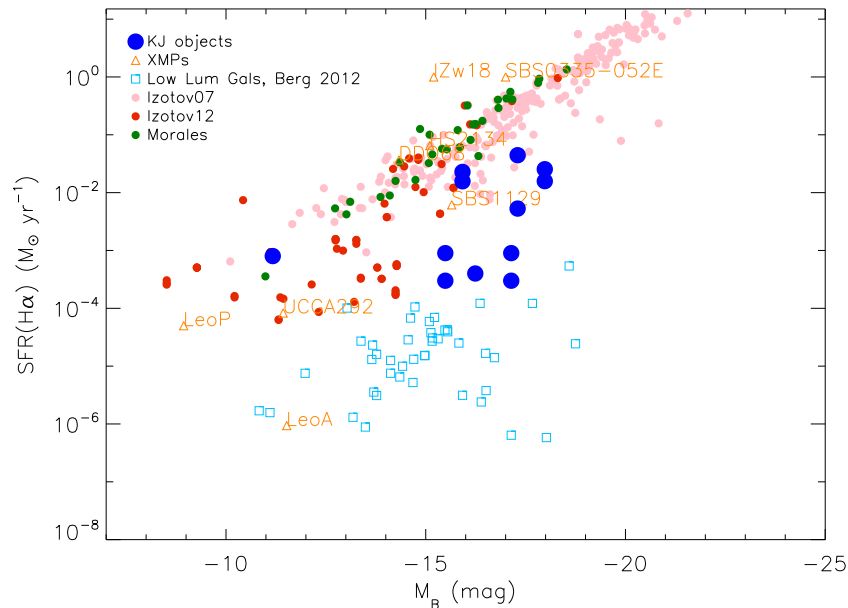


Figure 6. The relationship between absolute B -band magnitude (M_B) and SFR for our sample of BDD galaxies (i.e. KJ objects listed in Table 1). We also overplot the comparison sample described in Section 7.

and then every so often increase, and during this burst a dIrr may be classed as a BCD. However, if a starburst episode occurs within a BDD, their diffusely distributed H II regions would prevent it from displaying the compact characteristic of a BCD. This may in part be due to the method by which the star formation has been triggered within these systems. In BCDs, star formation is typically triggered by an inflow of H I gas (e.g. Gordon & Gottesman 1981; Zhao et al. 2013; Verbeke et al. 2014) and/or interaction or merging event (e.g. Pustilnik et al. 2001; Bekki 2008), causing star formation to occur in concentrated H II regions (see Sánchez Almeida et al. 2014 for an extensive review of this topic). In BDDs, however, we have star formation occurring in a less concentrated, haphazard distribution across each system.

The inflow of metal-poor gas into BCDs and other XMP galaxies has often been used to explain why these galaxies do not follow the $L-Z$ relationship seen in local star-forming dwarf galaxies. We illustrate this in Fig. 7, where we plot the B -band magnitudes and metallicities of low-luminosity galaxies and the $L-Z$ relationship of Berg et al. (2012), along with XMP galaxies of Morales-Luis et al. (2011), and other low-metallicity record holders (IZw 18, SBS 0335–052E, and Leo P). Pristine gas flowing into XMP and BCD galaxies not only depletes the interstellar medium (ISM) chemical abundances but also enables increased star-forming activity in and around the area of impact. In support of this, many of these outliers are known to have disturbed kinematics due to interaction and/or infall (van Zee et al. 1998; Ekta et al. 2006, 2008; Ekta, Pustilnik & Chengalur 2009). By contrast, Leo P and the BDD galaxies are in agreement with the $L-Z$ relation for local dwarf galaxies. Leo P is both extremely quiescent with regards to star formation and shows no signs of interaction and/or infall (Bernstein-Cooper et al. 2014), and is therefore thought have formed through normal evolution of low-mass galaxies (Skillman et al. 2013). Whilst BDDs are more actively star forming than Leo P and other low-luminosity galaxies (Fig. 6), the distribution of star-forming regions is still reminiscent of dIrrs, where star formation occurs in randomly distributed H II regions. However, in order to explore the possibility of inflowing metal-poor gas, we ultimately require integral field unit data.

Such observations can provide spatially resolved kinematics, velocity dispersions, and metallicities, and the combination of these three parameters can be used to recognize the presence of inflows or outflows (see e.g. James et al. 2013).

From the information currently available to us we propose that BDDs belong to a subclass of dIrrs which are forming stars more actively than typical dIrrs. Their distribution of star-forming regions (i.e. randomly scattered amongst a diffuse blue continuum, Fig. 1), low metallicities, and emission line ratios all suggest they are the diffuse counterparts to BCDs, where star formation occurs in smaller, more isolated H II regions, and under more ‘normal’ circumstances. It is this latter physical characteristic that has so far prevented them from being detected in emission line surveys. Our sample of objects shows that by focusing on a galaxy’s morphological properties, we can uncover alternatives to the bright, compact objects systematically found using traditional emission-line-based search techniques. Our results complement those of blind H I surveys, which are also largely successful in uncovering faint, blue cloud-like objects, and can reach down to very low mass objects (i.e. $\log M_{\text{HI}}/M_{\odot} < 7.7$; Huang et al. 2012). Whilst their metallicities are not as low as their model equivalent, Leo P, the fact that two out of eight objects can be classified as XMPs suggests that our morphology-based search technique may well be successful in filling in the missing low-metallicity dwarf galaxies. Upon reflection of our current sample, the range in metallicities and SFRs observed in BDDs suggests that (i) Leo P may well be an outlier with respect to these properties or (ii) our criteria are not efficient in selecting objects with metallicities as low as Leo P. However, both of these propositions are a consequence of distance (the two XMP galaxies uncovered via our search criteria are also the closest, i.e. within 7 Mpc) and without a specific volume-limited survey, we cannot fully assess the density/frequency of such extreme objects.

10 CONCLUSIONS

With the aim of uncovering rare XMP galaxies in the local Universe, we undertook a morphological-based search on SDSS

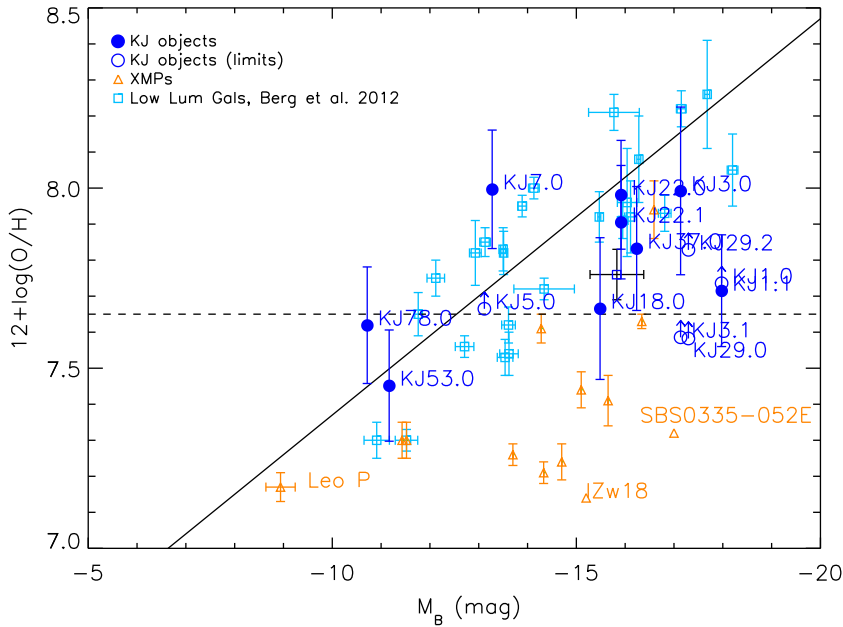


Figure 7. The relationship between oxygen abundance and absolute B -band magnitude (M_B) for our sample of BDD galaxies (i.e. KJ objects listed in Table 1). We also overplot the comparison sample described in Section 7.

imaging data, using the structural properties of the recently discovered XMP galaxy, Leo P, as a guide. Our unique search algorithm yielded ~ 100 blue, diffuse galaxies containing one or more H II regions embedded in low surface brightness emission; we have termed these objects BDD galaxies.

In this first report, we have presented preliminary results from ongoing optical spectroscopic follow-up observations of the BDD galaxies using the MMT spectrograph. The 12 galaxies discussed here lie at distances of ~ 5 –120 Mpc and ~ 40 arcsec across. We were able to extract separate spectra from multiple H II regions within five of the galaxies. All of the spectra showed bright emission lines typical of star-forming galaxies, with the exception of three objects (KJ 29.1, 32.0, and 80.0), which were excluded from further analysis. The final spectroscopic sample available for analysis consisted of a total of 15 spectra from 10 galaxies. The main results are as follows.

(i) Electron temperature measurements were achieved for nine out of 15 spectra, amounting to eight out of 10 galaxies, and for these we were able to derive ‘direct’ measurements of oxygen abundances. The systems were found to have metallicities in the range $7.45 < 12 + \log(\text{O}/\text{H}) < 8.0$. Two of the galaxies fall within the common definition of XMPs with $12 + \log(\text{O}/\text{H}) < 7.65$ (less than 1/10 solar).

(ii) Nitrogen-to-oxygen ratios were found to be in the range $-1.60 < \log(\text{N}/\text{O}) < -1.39$; such ratios are typical for the above values of oxygen abundance.

(iii) The galaxies we have observed exhibit current rates of star formation (derived from $H\alpha$ luminosities) ranging between 0.03×10^{-2} and $7.8 \times 10^{-2} M_{\odot} \text{ yr}^{-1}$.

(iv) The ages of the stellar populations responsible for the star formation we see are between 4.3 and 9.6 Myr, with a mean age of ~ 7 Myr.

(v) Because of their diffuse morphology, peak surface brightness estimates were not obtainable from SDSS images. However, we do

estimate the effective surface brightness, μ_B , to lie between 23 and 25 mag arcsec $^{-2}$. Absolute B -band magnitudes, M_B , are between ~ -11 and ~ -18 mag.

Overall, from the information gained on this subsample, BDDs appear to be a population of dwarf galaxies that lie in between the quiescent dIrrs and starbursting blue compact galaxies. Both their surface brightnesses and SFRs are intermediate between these two dwarf categories, suggesting that BDDs may represent more ‘normal’ metal-poor star-forming systems. However, in order to quantify and classify these galaxies fully, we will require additional data at a range of wavelengths. In particular, spatially resolved observations would be critical in obtaining kinematical information, whilst IR imaging would enable us to measure their mass.

If we return to the original motivation of this work, i.e. whether XMP galaxies are more readily detected if we focus on their diffuse ‘Leo P-type’ morphology, we have shown that while morphology-based searches have the ability to uncover objects that are *similar* to Leo P, objects with metallicities as low as Leo P appear to be extremely rare. We defer further discussion of this point to a future paper, once we have observed spectroscopically a larger fraction of our sample of BDDs.

We have demonstrated that searching for XMP galaxies using only their emission line properties may be preferentially biased towards finding those currently or recently undergoing a burst of star formation, or with star formation occurring in compactly distributed H II regions. By instead focusing on their optical morphological properties, we have uncovered metal-poor galaxies in which star formation is ongoing in isolated H II regions distributed within a diffuse continuum – a structural property which can lead to such galaxies being overlooked by most emission line searches.

ACKNOWLEDGEMENTS

Observations reported here were obtained at the MMT Observatory, a joint facility of the University of Arizona and the Smithsonian

Institution. We are grateful to the University of Arizona Observatory time assignment committee who awarded time to this programme, and thank the MMT telescope operators and staff for technical support. We are indebted to Alis Deason for providing the first-look spectroscopic observations of a subset of our sample that were used to support our initial MMT proposal. It is a pleasure to acknowledge Rob Kennicutt for useful discussions concerning dwarf galaxy populations, Matt Auger who helped with various aspects of the data analysis, and Evan Skillman for insightful comments on an early version of this work. We sincerely thank the reviewer of the paper, Jorge Sanchez Almeida, whose helpful comments and suggestions greatly improved the paper. EWO is partially supported by NSF grant AST1313006. The research leading to these results has received funding from the European Research Council under the European Union's Seventh Framework Programme (FP/2007-2013)/ERC Grant Agreement No. 308024. SK acknowledges financial support from the ERC. This research has made use of the NASA/IPAC Extragalactic Database (NED) which is operated by the Jet Propulsion Laboratory, California Institute of Technology, under contract with the National Aeronautics and Space Administration.

REFERENCES

- Ahn C. P. et al., 2012, *ApJS*, 203, 21
 Aloisi A. et al., 2007, *ApJ*, 667, L151
 Amorín R., Pérez-Montero E., Vílchez J. M., Papaderos P., 2012, *ApJ*, 749, 185
 Asplund M., Grevesse N., Sauval A. J., Scott P., 2009, *ARA&A*, 47, 481
 Baldwin J. A., Phillips M. M., Terlevich R., 1981, *PASP*, 93, 5
 Bekki K., 2008, *MNRAS*, 388, L10
 Bell E. F., McIntosh D. H., Katz N., Weinberg M. D., 2003, *ApJS*, 149, 289
 Berg D. A. et al., 2012, *ApJ*, 754, 98
 Bernstein-Cooper E. Z. et al., 2014, *AJ*, 148, 35
 Brinchmann J., Kunth D., Durret F., 2008, *A&A*, 485, 657
 Cannon J. M. et al., 2011, *ApJ*, 739, L22
 Coe D. et al., 2013, *ApJ*, 762, 32
 Cole A. A. et al., 2007, *ApJ*, 659, L17
 Cole A. A., Weisz D. R., Dolphin A. E., Skillman E. D., McConnachie A. W., Brooks A. M., Leaman R., 2014, *ApJ*, 795, 54
 Dopita M. A., Sutherland R. S., Nicholls D. C., Kewley L. J., Vogt F. P. A., 2013, *ApJS*, 208, 10
 Ekta B., Chengalur J. N., 2010, *MNRAS*, 406, 1238
 Ekta B., Chengalur J. N., Pustilnik S. A., 2006, *MNRAS*, 372, 853
 Ekta B., Chengalur J. N., Pustilnik S. A., 2008, *MNRAS*, 391, 881
 Ekta B., Pustilnik S. A., Chengalur J. N., 2009, *MNRAS*, 397, 963
 Ellis R. S. et al., 2013, *ApJ*, 763, L7
 Fitzpatrick E. L., 1999, *PASP*, 111, 63
 Garnett D. R., 1990, *ApJ*, 363, 142
 Garnett D. R., 2002, *ApJ*, 581, 1019
 Gil de Paz A., Madore B. F., Pevunova O., 2003, *ApJS*, 147, 29
 Giovanelli R. et al., 2005, *AJ*, 130, 2598
 Giovanelli R. et al., 2013, *AJ*, 146, 15
 Gordon D., Gottesman S. T., 1981, *AJ*, 86, 161
 Guseva N. G., Papaderos P., Izotov Y. I., Green R. F., Fricke K. J., Thuan T. X., Noeske K. G., 2003, *A&A*, 407, 75
 Haynes M. P. et al., 2011, *AJ*, 142, 170
 Huang S., Haynes M. P., Giovanelli R., Brinchmann J., 2012, *ApJ*, 756, 113
 Izotov Y. I., Thuan T. X., 1999, *ApJ*, 511, 639
 Izotov Y. I., Thuan T. X., Guseva N. G., 2005, *ApJ*, 632, 210
 Izotov Y. I., Stasińska G., Meynet G., Guseva N. G., Thuan T. X., 2006, *A&A*, 448, 955
 Izotov Y. I., Thuan T. X., Stasińska G., 2007, *ApJ*, 662, 15
 Izotov Y. I., Thuan T. X., Guseva N. G., 2012, *A&A*, 546, A122
 James B. L., Tsamis Y. G., Barlow M. J., Walsh J. R., Westmoquette M. S., 2013, *MNRAS*, 428, 86
 James B. L. et al., 2014, *MNRAS*, 440, 1794
 Karachentsev I. D., Makarov D. I., Kaisina E. I., 2013, *AJ*, 145, 101
 Kennicutt R. C., Jr, 1998, *ARA&A*, 36, 189
 Kewley L. J., Dopita M. A., 2002, *ApJS*, 142, 35
 Kewley L. J., Dopita M. A., Sutherland R. S., Heisler C. A., Trevena J., 2001, *ApJ*, 556, 121
 Kingsburgh R. L., Barlow M. J., 1994, *MNRAS*, 271, 257
 Koposov S., Bartunov O., 2006, in Gabriel C., Arviset C., Ponz D., Enrique S., eds, *ASP Conf. Ser. Vol. 351, Astronomical Data Analysis Software and Systems XV*. Astron. Soc. Pac., San Francisco, p. 735
 Lee H., Skillman E. D., Cannon J. M., Jackson D. C., Gehrz R. D., Polomski E. F., Woodward C. E., 2006, *ApJ*, 647, 970
 Legrand F., Kunth D., Roy J.-R., Mas-Hesse J. M., Walsh J. R., 2000, *A&A*, 355, 891
 Leitherer C., Ortiz Otálvaro P. A., Bresolin F., Kudritzki R.-P., Lo Faro B., Pauldrach A. W. A., Pettini M., Rix S. A., 2010, *ApJS*, 189, 309
 Lequeux J., Peimbert M., Rayo J. F., Serrano A., Torres-Peimbert S., 1979, *A&A*, 80, 155
 López-Sánchez Á. R., Esteban C., 2010a, *A&A*, 516, A104
 López-Sánchez Á. R., Esteban C., 2010b, *A&A*, 517, A85
 Lupton R., 2005, Transformations Between SDSS Magnitudes and UBVRI. <http://classic.sdss.org/dr7/algorithms/sdssUBVRITransform.html>
 Makarov D., Prugniel P., Terekhova N., Courtois H., Vauglin I., 2014, *A&A*, 570, A13
 McQuinn K. B. W. et al., 2013, *AJ*, 146, 145
 Morales-Luis A. B., Sánchez Almeida J., Aguerri J. A. L., Muñoz-Tuñón C., 2011, *ApJ*, 743, 77
 Nicholls D. C., Dopita M. A., Sutherland R. S., Jerjen H., Kewley L. J., Basurah H., 2014, *ApJ*, 786, 155
 Oesch P. A. et al., 2013, *ApJ*, 773, 75
 Papaderos P., Guseva N. G., Izotov Y. I., Fricke K. J., 2008, *A&A*, 491, 113
 Pettini M., Zych B. J., Steidel C. C., Chaffee F. H., 2008, *MNRAS*, 385, 2011
 Planck Collaboration I, 2014, *A&A*, 571, A1
 Pustilnik S. A., Brinks E., Thuan T. X., Lipovetsky V. A., Izotov Y. I., 2001, *AJ*, 121, 1413
 Pustilnik S. A., Kniazev A. Y., Pramskij A. G., 2005, *A&A*, 443, 91
 Pustilnik S. A., Engels D., Kniazev A. Y., Pramskij A. G., Ugryumov A. V., Hagen H.-J., 2006, *Astron. Lett.*, 32, 228
 Rhode K. L. et al., 2013, *AJ*, 145, 149
 Sánchez Almeida J., Muñoz-Tuñón C., Elmegreen D. M., Elmegreen B. G., Méndez-Abreu J., 2013, *ApJ*, 767, 74
 Sánchez Almeida J., Elmegreen B. G., Muñoz-Tuñón C., Elmegreen D. M., 2014, *A&AR*, 22, 71
 Schaerer D., Vacca W. D., 1998, *ApJ*, 497, 618
 Shirazi M., Brinchmann J., 2012, *MNRAS*, 421, 1043
 Skillman E. D., Kennicutt R. C., Hodge P. W., 1989, *ApJ*, 347, 875
 Skillman E. D., Côté S., Miller B. W., 2003, *AJ*, 125, 610
 Skillman E. D. et al., 2013, *AJ*, 146, 3
 Skillman E. D. et al., 2014, *ApJ*, 786, 44
 Tollerud E. J., Geha M. C., Grcevich J., Putman M. E., Stern D., 2015, *ApJ*, 798, L21
 van Zee L., 2000a, *ApJ*, 543, L31
 van Zee L., 2000b, *AJ*, 119, 2757
 van Zee L., Haynes M. P., 2006, *ApJ*, 636, 214
 van Zee L., Westpfahl D., Haynes M. P., Salzer J. J., 1998, *AJ*, 115, 1000
 Veilleux S., Osterbrock D. E., 1987, *ApJS*, 63, 295
 Verbeke R., De Rijcke S., Koleva M., Cloet-Osselaer A., Vandenbroucke B., Schroyen J., 2014, *MNRAS*, 442, 1830
 Vila Costas M. B., Edmunds M. G., 1993, *MNRAS*, 265, 199
 Zafar T., Centurión M., Péroux C., Molaro P., D'Odorico V., Vladilo G., Popping A., 2014, *MNRAS*, 444, 744
 Zhao Y., Gao Y., Gu Q., 2013, *ApJ*, 764, 44
 Zheng W. et al., 2012, *Nature*, 489, 406

APPENDIX A: OBSERVED FLUXES AND LINE INTENSITIES**Table A1.** Spectroscopic line fluxes and dereddened line intensities (both relative to $H\beta = 100$) as measured from the spectra shown in Fig. 2.

	KJ 1.0		KJ 1.1		KJ 3.0		KJ 3.1	
[O II] 3727.10	170 ± 27	199 ± 33	70.0 ± 10.2	70.0 ± 10.2	58.3 ± 12.9	58.3 ± 12.9	212 ± 32	222 ± 33
[O II] 3729.86	140 ± 23	164 ± 27	57.3 ± 8.3	57.3 ± 8.3	101 ± 22	101 ± 22	193 ± 29	202 ± 30
He I 3820.84	–	–	–	–	–	–	–	–
[Ne III] 3870.16	41.9 ± 8.5	47.9 ± 9.7	33.5 ± 4.8	33.5 ± 4.8	33.1 ± 7.3	33.1 ± 7.3	–	–
He I+H8 3889.75	–	–	19.1 ± 2.8	19.1 ± 2.8	18.1 ± 4.0	18.1 ± 4.0	–	–
He II 3969.55	–	–	24.7 ± 3.6	24.7 ± 3.6	24.5 ± 5.4	24.5 ± 5.4	–	–
He I 4027.49	–	–	2.31 ± 0.74	2.31 ± 0.74	1.51 ± 0.42	1.51 ± 0.42	–	–
[S II] 4069.75	–	–	–	–	–	–	–	–
H δ 4102.89	–	–	24.3 ± 3.5	24.3 ± 3.5	24.9 ± 5.5	24.9 ± 5.5	–	–
H γ 4341.68	–	–	43.9 ± 6.3	43.9 ± 6.3	46.1 ± 10.2	46.1 ± 10.2	54.8 ± 9.1	55.9 ± 9.3
[O III] 4364.44	<9.33	<9.95	10.4 ± 1.6	10.4 ± 1.6	7.95 ± 1.78	7.95 ± 1.78	<6.95	<7.09
He I 4472.93	–	–	4.68 ± 0.91	4.68 ± 0.91	3.81 ± 0.88	3.81 ± 0.88	–	–
Fe III 4659.35	–	–	–	–	–	–	–	–
He II 4687.02	–	–	2.12 ± 0.64	2.12 ± 0.64	–	–	–	–
Ar IV 4741.49	–	–	–	–	–	–	–	–
H β 4862.72	100 ± 15	100 ± 15	100 ± 14	100 ± 14	100 ± 22	100 ± 22	100 ± 15	100 ± 15
[O III] 4960.29	118 ± 18	117 ± 18	154 ± 21	154 ± 21	174 ± 38	174 ± 38	68.9 ± 10.7	68.7 ± 10.7
[O III] 5008.24	362 ± 54	355 ± 54	477 ± 67	477 ± 67	528 ± 116	528 ± 116	207 ± 30	206 ± 30
[N II] 5756.24	–	–	–	–	–	–	–	–
He I 5877.59	–	–	8.46 ± 1.35	8.46 ± 1.35	10.0 ± 2.2	10.0 ± 2.2	–	–
[O I] 6302.05	–	–	2.04 ± 0.61	2.04 ± 0.61	2.77 ± 0.65	2.77 ± 0.65	–	–
[S III] 6313.80	–	–	–	–	1.51 ± 0.39	1.51 ± 0.39	–	–
[O I] 6365.54	–	–	–	–	–	–	–	–
H α 6564.61	335 ± 50	286 ± 43	265 ± 37	265 ± 37	256 ± 56	256 ± 56	346 ± 51	329 ± 48
[N II] 6585.20	<8.29	<7.06	4.76 ± 0.89	4.76 ± 0.89	6.00 ± 1.35	6.00 ± 1.35	25.1 ± 5.2	23.9 ± 4.9
He I 6679.99	40.1 ± 8.8	33.9 ± 7.5	7.84 ± 1.41	7.84 ± 1.41	2.61 ± 0.61	2.61 ± 0.61	–	–
[S II] 6718.29	49.3 ± 9.1	41.6 ± 7.7	10.3 ± 1.6	10.3 ± 1.6	12.6 ± 2.8	12.6 ± 2.8	55.1 ± 9.8	52.4 ± 9.3
[S II] 6732.67	29.1 ± 7.3	24.5 ± 6.1	8.98 ± 1.44	8.98 ± 1.44	10.0 ± 2.2	10.0 ± 2.2	40.3 ± 7.1	38.3 ± 6.8
[Ne III] 6870.16	–	–	–	–	–	–	–	–
[Ar III] 7137.80	–	–	2.23 ± 0.71	2.23 ± 0.71	6.20 ± 1.40	6.20 ± 1.40	14.3 ± 5.1	13.5 ± 4.8
[O II] 7321.47	52.5 ± 10.4	42.6 ± 8.6	6.66 ± 1.29	6.66 ± 1.29	2.40 ± 0.59	2.40 ± 0.59	19.5 ± 4.8	18.3 ± 4.5
[O II] 7332.25	–	–	–	–	0.82 ± 0.25	0.82 ± 0.25	–	–
$F(H\beta) \times 10^{-16} \text{ erg s}^{-1} \text{ cm}^{-2}$	3.63 ± 0.41		20.5 ± 2.1		36.1 ± 5.6		2.81 ± 0.30	
$I(H\beta) \times 10^{-16} \text{ erg s}^{-1} \text{ cm}^{-2}$	6.02 ± 0.81		20.5 ± 2.1		36.1 ± 5.9		3.27 ± 0.36	
$E(B - V)$	0.15 ± 0.02		0.00 ± 0.00		0.00 ± 0.01		0.05 ± 0.01	

Table A1. – continued

	KJ 5.0		KJ 7.0		KJ 18.0		KJ 18.1	
[O II] 3727.10	91.2 ± 13.8	110.0 ± 16.8	136 ± 19	148 ± 21	110 ± 16	128 ± 19	408 ± 70	528 ± 94
[O II] 3729.86	105 ± 15	127 ± 19	78.0 ± 11.3	85.2 ± 12.4	86.7 ± 12.9	101.3 ± 15.2	179 ± 35	232 ± 47
He I 3820.84	12.1 ± 2.6	14.3 ± 3.1	–	–	5.79 ± 1.71	6.66 ± 1.97	111 ± 21	140 ± 27
[Ne III] 3870.16	8.43 ± 1.92	9.91 ± 2.26	26.7 ± 3.9	28.8 ± 4.2	23.3 ± 3.6	26.6 ± 4.1	38.5 ± 10.0	48.0 ± 12.6
He I+H8 3889.75	7.60 ± 2.29	8.92 ± 2.69	14.5 ± 2.2	15.6 ± 2.4	15.9 ± 2.9	18.1 ± 3.3	–	–
He II 3969.55	7.42 ± 1.94	8.58 ± 2.25	19.5 ± 2.9	20.9 ± 3.1	12.0 ± 2.2	13.5 ± 2.5	–	–
He I 4027.49	–	–	–	–	–	–	–	–
[S II] 4069.75	–	–	2.90 ± 0.87	3.08 ± 0.93	–	–	–	–
H δ 4102.89	16.9 ± 2.9	19.0 ± 3.3	22.6 ± 3.3	24.0 ± 3.5	20.2 ± 3.2	22.3 ± 3.6	–	–
H γ 4341.68	37.3 ± 6.1	40.5 ± 6.7	41.1 ± 5.9	42.7 ± 6.1	39.3 ± 5.9	42.0 ± 6.4	–	–
[O III] 4364.44	<2.66	<2.88	4.86 ± 0.99	5.04 ± 1.02	6.45 ± 1.60	6.88 ± 1.71	<15.2	<16.9
He I 4472.93	5.32 ± 1.68	5.65 ± 1.78	3.33 ± 0.76	3.43 ± 0.79	–	–	–	–
Fe III 4659.35	–	–	–	–	–	–	–	–
He II 4687.02	–	–	2.08 ± 0.63	2.11 ± 0.64	–	–	–	–
Ar IV 4741.49	–	–	–	–	–	–	–	–
H β 4862.72	100.0 ± 14.4	100.0 ± 14.4	100 ± 14	100 ± 14	100 ± 14	100 ± 14	100 ± 18	100 ± 18
[O III] 4960.29	43.7 ± 6.5	43.0 ± 6.4	112 ± 16	112 ± 15	94.0 ± 13.5	92.8 ± 13.3	63.3 ± 19.5	62.0 ± 19.1
[O III] 5008.24	132 ± 19	129 ± 18	341 ± 48	338 ± 47	283 ± 40	279 ± 39	188 ± 34	183 ± 33
[N II] 5756.24	–	–	–	–	–	–	–	–
He I 5877.59	10.5 ± 2.5	9.3 ± 2.2	9.33 ± 1.62	8.80 ± 1.53	11.0 ± 2.0	9.9 ± 1.8	–	–
[O I] 6302.05	–	–	3.19 ± 0.68	2.95 ± 0.63	6.91 ± 1.47	6.02 ± 1.29	–	–
[S III] 6313.80	–	–	1.72 ± 0.61	1.59 ± 0.57	–	–	–	–
[O I] 6365.54	–	–	2.42 ± 0.60	2.24 ± 0.55	–	–	–	–
H α 6564.61	309 ± 44	256 ± 37	292 ± 41	267 ± 37	308 ± 44	263 ± 37	371 ± 61	285 ± 48
[N II] 6585.20	7.01 ± 1.57	5.79 ± 1.31	13.0 ± 1.9	11.9 ± 1.8	8.53 ± 1.55	7.27 ± 1.33	44.1 ± 10.3	33.9 ± 8.0
He I 6679.99	–	–	3.67 ± 0.68	3.35 ± 0.62	3.70 ± 0.99	3.14 ± 0.84	24.5 ± 7.6	18.6 ± 5.8
[S II] 6718.29	21.1 ± 3.3	17.2 ± 2.7	28.1 ± 4.0	25.6 ± 3.7	24.1 ± 3.6	20.4 ± 3.1	94.9 ± 17.0	71.9 ± 13.3
[S II] 6732.67	11.1 ± 1.9	9.0 ± 1.6	20.7 ± 3.0	18.8 ± 2.7	18.7 ± 2.8	15.8 ± 2.4	54.3 ± 11.0	41.1 ± 8.5
[Ne III] 6870.16	–	–	1.35 ± 0.47	1.22 ± 0.43	–	–	–	–
[Ar III] 7137.80	5.74 ± 1.32	4.53 ± 1.05	6.52 ± 1.03	5.83 ± 0.92	6.58 ± 1.22	5.41 ± 1.01	22.1 ± 7.0	16.0 ± 5.1
[O II] 7321.47	–	–	–	–	–	–	–	–
[O II] 7332.25	6.55 ± 1.84	5.09 ± 1.44	–	–	4.10 ± 1.12	3.33 ± 0.91	27.6 ± 8.8	19.5 ± 6.3
$F(\text{H}\beta) \times 10^{-16} \text{ erg s}^{-1} \text{ cm}^{-2}$	7.06 ± 0.72		19.2 ± 1.9		6.74 ± 0.68		1.43 ± 0.19	
$I(\text{H}\beta) \times 10^{-16} \text{ erg s}^{-1} \text{ cm}^{-2}$	13.0 ± 1.7		25.5 ± 2.7		11.1 ± 1.3		3.27 ± 0.61	
$E(B - V)$	0.18 ± 0.02		0.09 ± 0.01		0.15 ± 0.02		0.25 ± 0.04	

Table A1. – *continued*

	KJ 22.0		KJ 22.1		KJ 29.0		KJ 29.2	
[O II] 3727.10	66.4 ± 9.5	76.1 ± 11.0	64.2 ± 9.3	73.6 ± 10.7	87.7 ± 13.6	95.9 ± 15.0	87.3 ± 13.3	102.4 ± 15.7
[O II] 3729.86	71.6 ± 10.3	82.0 ± 11.8	80.2 ± 11.5	92.0 ± 13.3	97.6 ± 15.0	106.7 ± 16.5	79.4 ± 12.2	93.1 ± 14.4
He I 3820.84	–	–	–	–	–	–	7.19 ± 2.14	8.31 ± 2.47
[Ne III] 3870.16	32.3 ± 4.6	36.3 ± 5.2	31.1 ± 4.5	35.0 ± 5.1	10.4 ± 2.5	11.3 ± 2.7	110 ± 16	126 ± 18
He I+H8 3889.75	13.9 ± 2.1	15.6 ± 2.3	13.4 ± 2.0	15.0 ± 2.3	12.4 ± 2.8	13.4 ± 3.0	–	–
He II 3969.55	21.2 ± 3.1	23.6 ± 3.4	20.5 ± 3.0	22.8 ± 3.4	–	–	11.0 ± 2.5	12.4 ± 2.8
He I 4027.49	2.15 ± 0.62	2.38 ± 0.68	–	–	–	–	–	–
[S II] 4069.75	–	–	–	–	–	–	–	–
H δ 4102.89	21.7 ± 3.1	23.7 ± 3.4	22.3 ± 3.3	24.4 ± 3.6	12.0 ± 2.6	12.7 ± 2.8	19.5 ± 3.3	21.7 ± 3.7
H γ 4341.68	43.0 ± 6.1	45.6 ± 6.5	41.3 ± 5.9	43.8 ± 6.3	44.2 ± 6.8	45.9 ± 7.1	41.3 ± 6.3	44.3 ± 6.8
[O III] 4364.44	7.19 ± 1.16	7.61 ± 1.22	7.18 ± 1.25	7.60 ± 1.32	<3.44	<3.57	<2.76	<2.95
He I 4472.93	3.75 ± 0.70	3.92 ± 0.73	4.50 ± 0.89	4.70 ± 0.93	–	–	–	–
Fe III 4659.35	–	–	–	–	–	–	–	–
He II 4687.02	2.11 ± 0.55	2.16 ± 0.56	–	–	6.36 ± 1.95	6.45 ± 1.97	–	–
Ar IV 4741.49	–	–	–	–	–	–	–	–
H β 4862.72	100 ± 14	100 ± 14	100 ± 14	100 ± 14	100 ± 14	100 ± 14	100 ± 14	100 ± 14
[O III] 4960.29	171 ± 24	169 ± 24	153 ± 21	151 ± 21	51.2 ± 7.7	50.9 ± 7.7	63.2 ± 9.3	62.4 ± 9.2
[O III] 5008.24	512 ± 72	504 ± 71	458 ± 64	451 ± 64	151 ± 22	149 ± 21	182 ± 26	179 ± 25
[N II] 5756.24	–	–	–	–	–	–	–	–
He I 5877.59	11.1 ± 1.7	10.1 ± 1.5	12.6 ± 2.0	11.5 ± 1.8	8.81 ± 2.49	8.30 ± 2.35	12.7 ± 2.6	11.4 ± 2.4
[O I] 6302.05	3.60 ± 0.70	3.19 ± 0.62	2.09 ± 0.68	1.85 ± 0.61	–	–	–	–
[S III] 6313.80	2.00 ± 0.57	1.77 ± 0.50	–	–	–	–	–	–
[O I] 6365.54	1.49 ± 0.49	1.31 ± 0.43	–	–	–	–	4.27 ± 1.48	3.69 ± 1.28
H α 6564.61	322 ± 45	281 ± 40	313 ± 44	272 ± 38	309 ± 44	282 ± 41	322 ± 46	274 ± 39
[N II] 6585.20	8.65 ± 1.35	7.52 ± 1.18	6.84 ± 1.20	5.94 ± 1.05	6.42 ± 1.94	5.86 ± 1.77	<2.58	<2.19
He I 6679.99	4.35 ± 0.77	3.76 ± 0.67	3.92 ± 0.82	3.38 ± 0.71	11.8 ± 3.3	10.7 ± 3.0	10.2 ± 2.9	8.6 ± 2.5
[S II] 6718.29	21.6 ± 3.1	18.7 ± 2.7	19.0 ± 2.8	16.4 ± 2.4	13.6 ± 2.8	12.3 ± 2.5	11.1 ± 2.3	9.4 ± 2.0
[S II] 6732.67	13.9 ± 2.0	12.0 ± 1.8	13.6 ± 2.0	11.7 ± 1.8	11.4 ± 2.5	10.3 ± 2.3	14.1 ± 2.6	11.8 ± 2.2
[Ne III] 6870.16	–	–	–	–	–	–	–	–
[Ar III] 7137.80	7.11 ± 1.12	5.99 ± 0.95	6.76 ± 1.13	5.68 ± 0.95	–	–	–	–
[O II] 7321.47	2.62 ± 0.67	2.18 ± 0.56	–	–	5.38 ± 1.95	4.77 ± 1.73	–	–
[O II] 7332.25	3.52 ± 0.67	2.93 ± 0.56	2.79 ± 0.70	2.32 ± 0.58	–	–	–	–
$F(\text{H}\beta) \times 10^{-16} \text{ erg s}^{-1} \text{ cm}^{-2}$	24.0 ± 2.4		15.4 ± 1.5		4.44 ± 0.46		5.68 ± 0.59	
$I(\text{H}\beta) \times 10^{-16} \text{ erg s}^{-1} \text{ cm}^{-2}$	37.2 ± 4.2		24.0 ± 2.7		5.94 ± 0.65		9.51 ± 1.15	
$E(B - V)$	0.13 ± 0.01		0.13 ± 0.02		0.09 ± 0.01		0.16 ± 0.02	

Table A1. – continued

	KJ 37.0		KJ 53.0		KJ 78.0	
[O II] 3727.10	97.0 ± 14.0	130.0 ± 19.2	41.8 ± 6.0	42.0 ± 6.0	44.7 ± 6.6	45.1 ± 6.7
[O II] 3729.86	75.6 ± 11.0	101.3 ± 15.1	42.8 ± 6.1	43.0 ± 6.1	46.9 ± 6.9	47.3 ± 7.0
He I 3820.84	–	–	–	–	–	–
[Ne III] 3870.16	26.5 ± 3.9	34.0 ± 5.1	26.0 ± 3.7	26.1 ± 3.7	22.4 ± 3.3	22.6 ± 3.3
He I+H8 3889.75	12.0 ± 2.1	15.4 ± 2.7	17.9 ± 2.6	18.0 ± 2.6	16.8 ± 2.5	16.9 ± 2.5
He II 3969.55	14.4 ± 2.4	18.1 ± 3.0	20.0 ± 2.8	20.1 ± 2.9	20.7 ± 3.0	20.9 ± 3.1
He I 4027.49	–	–	1.24 ± 0.27	1.25 ± 0.27	2.48 ± 0.70	2.49 ± 0.71
[S II] 4069.75	–	–	0.80 ± 0.23	0.80 ± 0.23	2.23 ± 0.73	2.24 ± 0.73
Hδ 4102.89	13.8 ± 2.3	16.7 ± 2.7	24.1 ± 3.4	24.1 ± 3.4	23.3 ± 3.4	23.4 ± 3.4
Hγ 4341.68	38.8 ± 5.6	44.1 ± 6.4	45.1 ± 6.4	45.1 ± 6.4	41.8 ± 6.0	41.9 ± 6.0
[O III] 4364.44	7.63 ± 1.57	8.62 ± 1.77	8.93 ± 1.28	8.95 ± 1.29	7.46 ± 1.27	7.49 ± 1.27
He I 4472.93	–	–	3.18 ± 0.48	3.19 ± 0.48	3.15 ± 0.69	3.16 ± 0.69
Fe III 4659.35	–	–	–	–	–	–
He II 4687.02	–	–	–	–	–	–
Ar IV 4741.49	–	–	–	–	–	–
Hβ 4862.72	100 ± 14	100 ± 14	100 ± 14	99 ± 14	100 ± 14	99 ± 14
[O III] 4960.29	150 ± 21	146 ± 20	113 ± 15	113 ± 15	117 ± 16	117 ± 16
[O III] 5008.24	419 ± 59	406 ± 57	338 ± 47	338 ± 47	357 ± 50	357 ± 50
[N II] 5756.24	–	–	–	–	–	–
He I 5877.59	10.9 ± 2.2	8.9 ± 1.8	10.00 ± 1.43	9.98 ± 1.43	9.75 ± 1.60	9.69 ± 1.59
[O I] 6302.05	6.69 ± 1.42	5.16 ± 1.10	0.85 ± 0.22	0.84 ± 0.22	–	–
[S III] 6313.80	5.69 ± 1.34	4.38 ± 1.04	1.30 ± 0.25	1.30 ± 0.25	–	–
[O I] 6365.54	–	–	–	–	–	–
Hα 6564.61	368 ± 52	273 ± 40	280 ± 39	279 ± 39	265 ± 37	263 ± 37
[N II] 6585.20	12.5 ± 2.1	9.2 ± 1.6	2.83 ± 0.44	2.82 ± 0.44	4.68 ± 0.82	4.64 ± 0.81
He I 6679.99	–	–	3.02 ± 0.46	3.01 ± 0.45	2.54 ± 0.53	2.52 ± 0.52
[S II] 6718.29	34.0 ± 5.0	24.8 ± 3.7	6.83 ± 0.98	6.80 ± 0.98	6.31 ± 1.00	6.25 ± 0.99
[S II] 6732.67	22.8 ± 3.5	16.6 ± 2.6	5.04 ± 0.73	5.02 ± 0.73	5.33 ± 0.87	5.28 ± 0.86
[Ne III] 6870.16	–	–	–	–	–	–
[Ar III] 7137.80	10.8 ± 2.0	7.5 ± 1.4	4.03 ± 0.59	4.02 ± 0.59	5.00 ± 0.83	4.95 ± 0.82
[O II] 7321.47	–	–	1.21 ± 0.26	1.20 ± 0.25	–	–
[O II] 7332.25	3.89 ± 1.18	2.63 ± 0.81	1.60 ± 0.34	1.59 ± 0.34	2.94 ± 0.85	2.91 ± 0.84
$F(H\beta) \times 10^{-16} \text{ erg s}^{-1} \text{ cm}^{-2}$	9.11 ± 0.92		62.3 ± 6.2		26.7 ± 2.7	
$I(H\beta) \times 10^{-16} \text{ erg s}^{-1} \text{ cm}^{-2}$	23.4 ± 3.5		63.1 ± 6.3		27.4 ± 2.8	
$E(B - V)$	0.29 ± 0.03		0.00 ± 0.00		0.01 ± 0.00	

SUPPORTING INFORMATION

Additional Supporting Information may be found in the online version of this article:

All_fluxes_combined0v2.ascii

All_fluxes_combined1v2.ascii

All_fluxes_combined2v2.ascii

All_fluxes_combined3v2.ascii (<http://mnras.oxfordjournals.org/>

[lookup/suppl/doi:10.1093/mnras/stv175/-/DC1](http://mnras.oxfordjournals.org/lookup/suppl/doi:10.1093/mnras/stv175/-/DC1)).

Please note: Oxford University Press are not responsible for the content or functionality of any supporting materials supplied by the authors. Any queries (other than missing material) should be directed to the corresponding author for the article.

This paper has been typeset from a $\text{\TeX}/\text{\LaTeX}$ file prepared by the author.